A comparison of the vehicle vibration energy harvesting abilities of the regenerative shock absorbers predicted by the quarter, half and full vehicle suspension system models

Ran Zhang[a,b], Liya Zhao[c], Xiaojun Qiu[c], Hui Zhang[a*], Xu Wang[b*]

[a]School of Transport Engineering, Beijing University of Aeronautics and Astronautics, China

[b*]School of Engineering, RMIT University, Bundoora, VIC 3083, Australia

[c]School of Mechanical and Mechatronic Engineering, University of Technology Sydney,
Ultimo 2007, NSW, Australia

Abstract: Regenerative shock absorber has been studied intensively for generating electricity from motion energy that would have been otherwise dissipated and wasted in the form of heat. Integration of the regenerative shock absorber with the vehicle suspension system can incorporate the interaction between the wheels and vehicle body, resulting in more accurate power output results. Three vehicle suspension system models (the quarter, the half, and the full) are commonly applied in modelling and simulations, each of them having its advantages and disadvantages. However, these models have never been compared thoroughly for their feasibilities in evaluation of harvested motion energy. The quarter and half vehicle suspension system models have their own restrictions which limit their applications to certain road conditions. This paper presents the modellings of quarter, half and full vehicle suspension system models integrated with regenerative shock absorbers based on the same baseline vehicle. The time domain and frequency domain analyses enable a comprehensive comparison of all three models to be conducted in terms of the effects of vehicle speeds, position of vehicle center of gravity, road classifications (road class A, C and E) and driving speed cycles (NEDC, HWFET and FTD-75). The results suggest that the shift of vehicle center of gravity position does not affect the results of any suspension system models. All the three suspension system models can respond well to road classification change and rougher road can yield higher power output. The quarter vehicle suspension system model does not present accurate power output results at low frequencies, and behaves poorly with the vehicle speed variation, which limits its use to highway driving cycle HWFET. The half vehicle suspension system model resembles full vehicle suspension system model really well regardless of frequency ranges, vehicle speed variations and road classifications, when the transverse road profile is neglected.

Keywords: Regenerative shock absorber, quarter vehicle suspension system, half vehicle suspension system, full vehicle suspension system, vehicle speed, center of gravity position, road classification, driving speed cycle.

Nomenclature

m	Quarter vehicle body mass	l_f	Distance between the vehicle centre of gravity to front axle.
m_1	Quarter vehicle wheel assembly mass	l_b	Distance between the vehicle centre of gravity to rear axle.
m_{fr}	Front right wheel assembly mass	l_l	Absolute distance between the vehicle centre of gravity to the left wheels
m_{fl}	Front left wheel assembly mass	l_r	Absolute distance between the vehicle centre of gravity to the right wheels
m_{rl}	Rear left wheel assembly mass	i	Gear ratio
m_{rr}	Rear right wheel assembly mass	J	Rotational inertia of the half vehicle
$m_{1\mathrm{f}}$	Half vehicle front wheel assembly mass	J_{FW}	Rotational inertia of the flywheel
$m_{1\mathrm{r}}$	Half vehicle rear wheel assembly mass	Bl	The product of magnetic field intensity and coil length
m_2	Half vehicle body mass	J_{am}	Rotational inertia of the driving arm
m_{tp}	Top plate mass	J_{pcr}	Rotational inertia of the planetary gear carrier
m_{p}	Planetary gear mass	J_P	Rotational inertia of the planetary gear
m_s	Equivalent mass	J_g	Rotational inertia of the generator
m_b	Full vehicle body mass	J_s	Rotational inertia of the sun gear
k_{sfr}	Front right suspension stiffness	r_{P}	Planetary gear radius
k_{sfl}	Front left suspension stiffness	r	Equivalent rotational inertia radius
k_{srl}	Rear left suspension stiffness	r_g	Generator rotor radius
k_{srr}	Rear right suspension stiffness	R	Coil resistance
k_1	Tyre stiffness	R_{e}	External resistance
k_{1f}	Front tyre stiffness	L_e	Coil inductance
k_{1r}	Rear tyre stiffness	η_g	Efficiency of generator
k_2	Quarter vehicle suspension stiffness	k_e	Generator constant
k_{2f}	Half vehicle Front suspension stiffness	c_L	Equivalent damping of the differential gear box and DC generator

k_{2r}	Half vehicle Rear suspension stiffness	η_{tp}	Efficiency of top plate
c_{sfr}	Front right suspension damping	η_{pg}	Efficiency of planetary gear
c_{sfl}	Front left suspension damping	β	Rolling inertia of the full vehicle
c_{srr}	Rear right suspension damping	F_{LR}	Lorenz force
c_{srl}	Rear left suspension damping	F_{Gi}	Inertia force
c_{tfr}	Front right tyre damping	F_{Wi}	Damping force
c_{tfl}	Front left tyre damping	F_{Ki}	Spring restoring force
c_{trr}	Rear right tyre damping	n	Multiplication factor
c_{trl}	Rear left tyre damping	U	Generated voltage
c_1	Quarter vehicle tyre damping	U_f	Generated voltage of the front regenerative shock absorber
c_{1f}	Half vehicle Front tyre damping	U_r	Generated voltage of the rear regenerative shock absorber
c_{1r}	Half vehicle Rear tyre damping	U_{fr}	Generated voltage of the front right regenerative shock absorber
c_2	Quarter vehicle shock absorber damping	U_{fl}	Generated voltage of the front left regenerative shock absorber
c_{2f}	Half vehicle Front shock absorber damping	U_{rr}	Generated voltage of the rear right regenerative shock absorber
c_{2r}	Half vehicle Rear shock absorber damping	U_{rl}	Generated voltage of the rear left regenerative shock absorber
α	Pitching inertia of the full vehicle	θ	Pitching angle of the half vehicle
y	Road profile displacement under wheel	I_a	Pitching angle of the full vehicle
y_f	Road profile displacement under front wheel	I_b	Rolling angle of the full vehicle
y_r	Road profile displacement under rear wheel		
y_{tfr}	Road profile displacement under front right wheel		
y_{tfl}	Road profile displacement under front left wheel		
y_{trr}	Road profile displacement under rear right wheel	NEDC	New European Driving Cycle

y_{trl}	Road profile displacement under rear left wheel	HWFET	Highway Fuel Economy Test
y_b	Vehicle body displacement	FTD-75	Federal Test Procedure

1. Introduction

Due to the fact that demand for petroleum as vehicle fuel has been increasing dramatically, the dependency on the chemical energy in the petroleum has to be restricted and as a result, the alternative energy source will eventually draw more attentions. Within the petroleum, 84-90% of the chemical energy is wasted in the form of heat [1]. 75% of the energy loss is through the engine, while the wheel energy loss accounts for about 22.5% [2, 3]. The wheel energy loss is mainly attributed by rolling tires and shock absorber movement, where the energy loss of later has more potential to be converted into electrical energy because of its readiness for implementation. This has been realized through the use of the regenerative shock absorber, which incorporates electromagnetic motor to generate electricity.

In order for the electromagnetic motor to work properly, shock absorber linear motion will need to be converted into motor motion first. This can be achieved in two ways: direct-drive and indirect-drive [3]. Direct-drive regenerative shock absorbers (RSA) are equipped with linear motor which allows the linear motion to electricity conversion from the shock absorber to motor [4, 5, 6, 7, 8, 9, 10]. Indirect-drive RSA are equipped with rotary motor which requires the conversion of the linear motion of the shock absorber to rotary motion of the motor. The conversion can be realized through hydraulic pipe [11] [12] [13], rack and pinion mechanism [14, 15, 16, 17], arm-teeth mechanism [18, 19], ball screws mechanism [20, 21, 22, 23, 24, 25, 26] and etc. During the conversion process the motor rotation speed is always amplified.

In some studies, RSAs are directly evaluated on the test platform without considering the vehicle where the shock absorbers operate on [11, 13, 27, 28, 29]. For example, Goldner et al. [10] studied the energy recovery using RSA. In the research, the electromagnetic linear motor is excited by a rotating wheel with a bump. It investigated the power output of the RSA due to the direct base excitation. However, this subjectively ignores the influence of the suspension system and the associated modal resonance, which contributes a lot to shock absorber movement and thus the power output. As a result, the movement on the test platform cannot resembles the shock absorber movement on the actual vehicle, thus the power output cannot be accurately predicted.

In order to further investigate the feasibility of the RSAs, the vehicle suspension system (VSS) models are introduced, allowing for the RSA to be studied as a part of the vehicle suspensions system under the road excitement. The shock absorber movements are the result of the relative movement between the wheels and vehicle body, thus it is necessary for a suspension model to include the vehicle body mass, wheel assembly mass, shock absorber damping and stiffness, tire damping and stiffness. Because most vehicles are axially symmetrical, a full VSS model can be divided into two half VSS models or four quarter VSS models.

A quarter VSS model contains one set of suspension-wheel assembly and a quarter vehicle body. This has been studied in many researches due to its simplicity. Singh et al. [30] investigated a novel hydraulic RSA in the frequency domain. It can be found that the power output peak often occurs at the natural frequencies, as a results of vigorous shock movement [31]. Lin et al. [32] conducted the research on an energy-regenerative active suspension based on the quarter VSS model in time domain. Another advantage of the quarter VSS model is that it is easier to build for testing. Ding et al. [33] conducted the experiments on control of the RSA based on a built quarter VSS model with masses, springs and dampers.

The effects of vehicle speed and road profile have been studied based on the quarter VSS model [34]; however the interference between the movements of front wheel and rear wheel limits the prediction accuracy of the quarter VSS model. Therefore many studies have used a half VSS model to include the vehicle pitching motion mode [20, 35, 36]. Wei et al. [37] studied the energy dissipation on the front wheel and the rear wheel suspensions of a half VSS model over different types of road. It was found that average dissipated power increases with the both road smoothness and vehicle speed. These results, however, does not apply to the energy regeneration of the shock absorbers.

A full model contains four sets of wheel suspension assembly and a vehicle body, thus it can be seen as the closest to the real vehicle among the three VSS models. Abdelkareem et al. [38] analyzed the potential of energy harvesting using a full VSS model. Control system has also been developed based on the full VSS model integrated with the RSAs [39]. Despite of its advance in accuracy, there are only a few researches applying the full VSS model due to its complexity. It is believed by some researchers that quarter VSS model and half VSS model are excellent replacements of full VSS model in terms of energy output prediction from the RSAs.

To answer this question, some literatures compare the quarter VSS model with the half VSS model [35, 40, 41]. However, no conclusion has been drawn in regards to how these VSS models can be applied considering their feasibility and simplicity. Therefore, in this paper, a comprehensive comparison between the quarter, half and full VSS models is conducted based on the same vehicle baseline in both the frequency domain and time domain. The established numerical models for the VSS models allow the energy generating performance of the RSA to be analyzed taking into account the effect of vehicle speed, position of the vehicle center of gravity (also called “COG”), road classifications and vehicle driving speed cycles. The results will illustrate how these VSS models respond differently to realistic conditions and provide guidelines on the applicability of a specific VSS model.

2. The vehicle suspension system models

The quarter, half and full VSS models are integrated with the same RSAs and vehicle platform for fair comparisons, as shown in Figure 1. The parameters of the baseline vehicle are provided in Table 1. The harvesting electrical circuit of the RSA is shown in Figure 2. R is the internal coil resistance; R_e is the matching external resistance which is equal to the internal coil resistance, resulting in the maximum power output according to [4]; L_e is the coil inductance. The force equilibrium equation is given in Eq. (1).

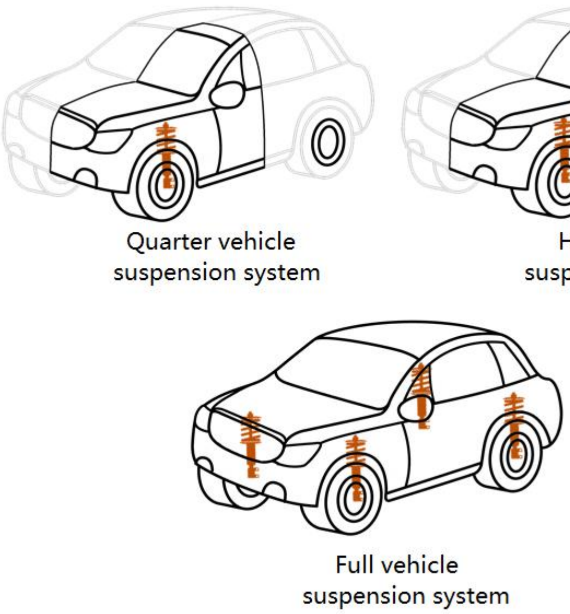

Figure 1: Schematic of quarter, half and full VSS model with the RSAs.

Table 1: Parameters of the vehicle.

Parameter	Value
Wheel assembly mass	40 kg
Vehicle body mass	1200 kg
Tyre stiffness	130000N/m
Suspension stiffness	26000 N/m
Tyre damping	264.7 Ns/m
Shock absorber damping	520 Ns/m
Vehicle wheel base	3.2 m
Vehicle width	1.4 m
Pitching inertia of the vehicle	3000 kg.m^2
Rolling inertia of the vehicle	574 kg.m^2

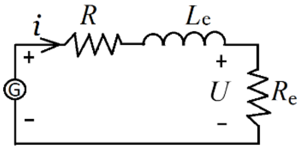

Figure 2: The harvesting electrical circuit of the RSA

$$\begin{cases} F_{LR} = Bl \cdot \dfrac{U}{R_e} \\ F_{Gi} + F_{Wi} + F_{Ki} \pm n \cdot F_{LR} = 0 \end{cases} \tag{1}$$

where F_{LR} is the Lorenz force resulting from moving coils in the magnetic field; F_{Gi}, F_{Wi}, and F_{Ki} are the inertia force, the damping force, and the spring restoring force of the i_{th} oscillator (i = 1, 2), respectively. Because of the gearbox, the Lorenz force F_{LR} induced torque is amplified when applied between the sprung mass and un-sprung mass and this multiplication factor is denoted as n [?]. Based on the Lagrange's equation, individual forces can be expressed as:

$$\begin{cases} F_{Gi} = \dfrac{d}{dt}\dfrac{\partial T}{\partial \dot{x}_i} - \dfrac{\partial T}{\partial x_i} \\ F_{Wi} = \dfrac{\partial W}{\partial \dot{x}_i} \\ F_{Ki} = \dfrac{\partial V}{\partial x_i} \end{cases} \tag{2}$$

Eq. (2) can be applied to all the VSS models for the derivation of the governing equations.

The relative movement between the wheel assembly and the vehicle body can initiate the operation of the RSA, and potentially higher road displacement can yield higher power output. The arm-teeth RSA in [19] is applied here on all the VSS models. The composition of the arm-teeth RSA includes the top plate, driving arms, flywheel, generator and the gear box consisting of planetary gear carrier, planetary gears, ring gear and sun gear, as shown in Figure 3. The downward motion of the top plate will engage the flywheel teeth to driving arms, which force the flywheel to rotate. When top plate moves upwards, the driving arms become disengaged with the flywheel teeth, allowing for the flywheel to continue spinning unidirectionally due to inertia.

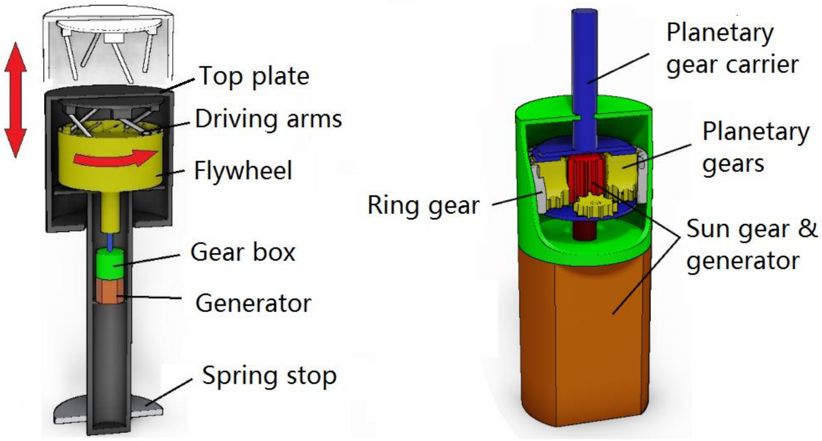

Figure 3: The composition of the regenerative shock absorber.

In order to accurately predict the operation performance of the arm-teeth RSA, the concept of the equivalent mass is introduced to represent the reciprocating mass of the top plate, flywheel, driving arms, planetary gear carrier, 4 planetary gears and the combination of the sun gear and the generator located after the gearbox. The flywheel, driving arms, planetary gear carriers and 4 planetary gears are rotating at the same angular velocity; the generator and the sun gear rotate faster than the rest of components due to the use of gearbox. c_L is the equivalent reciprocating damping of the combination of top plate, arm teeth mechanism, differential gear box and DC generator. The parameters of the RSA are given in Table 2.

Table 2: The parameters of the regenerative shock absorber.

Parameter		Value
Top plate mass	m_{tp}	3.72 kg
Planetary gear mass	m_{p}	0.049 kg
Coil resistance	R	10 Ω
External resistance	R_{e}	10 Ω
Coil inductance	L_e	9.4E-5 H
Gear ratio	i	22.6
Rotational inertia of the driving arm	J_{am}	1.92E-4 kg.m^2
Rotational inertia of the planetary gear carrier	J_{pcr}	5.6E-7 kg.m^2
Rotational inertia of the planetary gear	J_P	5.6E-7 kg.m^2
Rotational inertia of the generator	J_g	5.74E-6 kg.m^2
Rotational inertia of the sun gear	J_s	2.4E-7E-6 kg.m^2
Planetary gear radius	r_{P}	9.25E-3 m
Equivalent rotational inertia radius	r	3.268E-2 m
Generator rotor radius	r_g	0.01m
Equivalent damping of the differential gear box and DC generator	c_L	100 Ns/m
Efficiency of top plate	η_{tp}	92%
Efficiency of planetary gear	η_{pg}	80%
Efficiency of generator	η_g	65%
Generator constant	k_e	0.018

Therefore, equivalent mass m_s, equivalent damping coefficient c_L and motor constant k_e can be given by:

$$\begin{cases} m_s = m_{tp} + \dfrac{J_{FW} + J_{am} + J_{pcr} + 4\cdot\left(J_P + m_P \cdot r_P{}^2\right)}{r^2} + \dfrac{J_g + J_s}{r^2}\cdot i^2 \\ c_L = \dfrac{k_e{}^2 \cdot i^2}{r^2 \cdot \eta_{tp} \cdot \eta_{pg} \cdot \eta_g \cdot \left(R + R_e\right)} \\ k_e = Bl \cdot r_g \end{cases} \tag{3}$$

The lumped mass-spring dashpot models of the quarter, half and full VSSs are two degrees of freedom, four degrees of freedom and seven degrees of freedom, respectively. The RSAs are denoted as “G”, as shown in the schematics in Figures 4, 5 and 6. In order to apply the Langrage’s equation, the kinetic equations of the quarter, half and full VSS models are given in Eqs. (5), (7) and (9).

2.1 The quarter VSS model

The quarter VSS model has two degrees of freedom as shown in Figure 4, which consists of quarter vehicle mass m_0, wheel assembly mass m_1, suspension damping c_2, tire damping c_1, suspension stiffness k_2, tire stiffness k_1. The displacement variations of the quarter vehicle body and wheel assembly are x_2

and x_1, respectively.

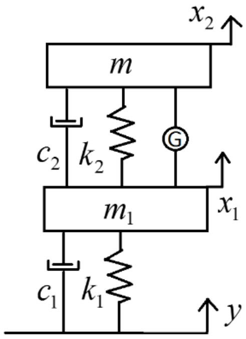

Figure 4: A quarter VSS model with the regenerative shock absorber.

The road profile displacement variation is y. The generated voltage is given by the product of the electromechanical coupling constant and coil velocity with respect to the magnet. Therefore, according to the RSA circuit shown in Figure 2, the generated electrical voltage balance equation of the RSA on the quarter VSS model can be expressed as:

$$L_e \cdot \frac{\dot{U}}{R_e} + \frac{U}{R_e} \cdot \left(R + R_e\right) = \frac{k_e \cdot i}{r} \cdot \left(x_1 - x_2\right) \tag{4}$$

The energy equations of the quarter VSS model is given in Eq. (5). Eq. (5) can be substituted back in Eq. (2) for the derivation of the equations of motion, which is shown in Appendix A. The equations of motion can be utilized for the energy harvesting analysis in both the frequency domain and the time domain.

$$\begin{cases} T = \frac{1}{2} \cdot m_s \cdot \left(\dot{x}_1 - \dot{x}_2\right)^2 + \frac{1}{2} \cdot m_1 \cdot \dot{x}_1^{\,2} + \frac{1}{2} m \cdot \dot{x}_2^{\,2} \\ W = \frac{1}{2} \cdot c_1 \cdot \left(\dot{x}_1 - \dot{y}\right)^2 + \frac{1}{2} \cdot c_2 \cdot \left(\dot{x}_1 - \dot{x}_2\right)^2 + \frac{1}{2} \cdot c_L \cdot \left(\dot{x}_1 - \dot{x}_2\right)^2 \\ V = \frac{1}{2} \cdot k_1 \cdot \left(x_1 - y\right)^2 + \frac{1}{2} \cdot k_2 \cdot \left(x_1 - x_2\right)^2 \end{cases} \tag{5}$$

2.2 The half VSS model

The half VSS model has four degrees of freedom as shown in Figure 5, which consists of half vehicle mass m_2, front wheel assembly mass m_{1f}, rear wheel assembly mass m_{1r}, front suspension stiffness k_{2f}, rear suspension stiffness k_{2r}, front suspension damping coefficient c_{2f}, rear suspension damping coefficient c_{2r}, front tire stiffness k_{1f}, rear tire stiffness k_{1r}, front tire damping coefficient c_{1f}, rear tire damping coefficient c_{1r}. The distance between the vehicle COG and the front and rear wheel axles are a and b, respectively. The pitching angle is denoted as θ. The half vehicle body displacement is x, the front tire displacement is x_f, the rear tire displacement is x_r, the front road profile displacement variation is y_f, the rear road profile displacement variation is y_r. The movement of the half VSS model involves pitching motion and therefore will be sensitive to the transverse road profile elevations.

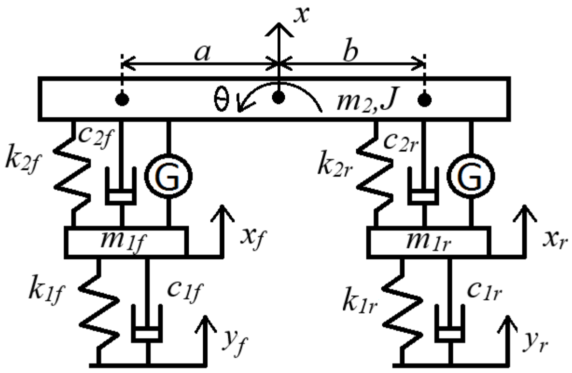

Figure 5: A half VSS model with the regenerative shock absorbers.

Similar to Eq. (5), the generated electric voltage balance equations of two RSAs on a half model are given by:

$$\begin{cases} L_e \cdot \dfrac{\dot{U}_f}{R} + \dfrac{U_f}{R} \cdot \left(R + R_e\right) = \dfrac{k_e \cdot i}{r} \cdot \left(\dot{x}_f - \dot{x} + l_f \dot{\theta}\right) \\ L_e \cdot \dfrac{\dot{U}_r}{R} + \dfrac{U_r}{R} \cdot \left(R + R_e\right) = \dfrac{k_e \cdot i}{r} \cdot \left(\dot{x}_r - \dot{x} - l_b \dot{\theta}\right) \end{cases} \tag{6}$$

The energy equations of the half VSS model is given in Eq. (7). Eq. (7) can be substituted back in Eq. (2) for the derivation of the equations of motion, which is shown in Appendix B.

$$\begin{cases} T = \dfrac{1}{2} m_s \left(\dot{x}_f - \dot{x} + l_f \dot{\theta}\right)^2 + \dfrac{1}{2} m_s \left(\dot{x}_r - \dot{x} - l_b \dot{\theta}\right)^2 + \dfrac{1}{2} m_2 \dot{x}^2 + \dfrac{1}{2} m_{1f} \dot{x}_f{}^2 + \dfrac{1}{2} m_{1r} \dot{x}_r{}^2 + \dfrac{1}{2} J \dot{\theta}^2 \\ W = \dfrac{1}{2} c_{1f} \left(\dot{y}_f - \dot{x}_f\right)^2 + \dfrac{1}{2} c_{1r} \left(\dot{y}_r - \dot{x}_r\right)^2 + \dfrac{1}{2} c_{2f} \left(\dot{x}_f - \dot{x} + l_f \dot{\theta}\right)^2 + \dfrac{1}{2} c_{2r} \left(\dot{x}_r - \dot{x} - l_b \dot{\theta}\right)^2 + \dfrac{1}{2} c_L \left[\left(\dot{x}_f - \dot{x} + l_f \dot{\theta}\right)^2 + \left(\dot{x}_r - \dot{x} - l_b \dot{\theta}\right)^2\right] \\ V = \dfrac{1}{2} k_{1f} \left(y_f - x_f\right)^2 + \dfrac{1}{2} k_{1r} \left(y_r - x_r\right)^2 + \dfrac{1}{2} k_{2f} \left(x_f - x + l_f \theta\right)^2 + \dfrac{1}{2} k_{2r} \left(x_r - x - l_b \theta\right)^2 \end{cases} \tag{7}$$

2.3 The full VSS model

The full VSS model has seven degrees of freedom as shown in Figure 6. It consists of vehicle mass m_b; front left, front right, rear left, rear right wheel assembly mass m_{fl}, m_{fr}, m_{rl}, m_{rr}; front left, front right, rear left, rear right suspension stiffness k_{sfl}, k_{sfr}, k_{srl}, k_{srr}; front left, front right, rear left, rear right suspension damping coefficient c_{sfl}, c_{sfr}, c_{srl}, c_{srr}; front left, front right, rear left, rear right tire stiffness k_{tfl}, k_{tfr}, k_{trl}, k_{trr}; front left, front right, rear left, rear right tire damping coefficient c_{tfl}, c_{tfr}, c_{trl}, c_{trr}; pitching angle α, rolling angle β; distance from the center of gravity to front and rear axial l_f and l_b; distance from the center of gravity to left and right axial l_l and l_r.

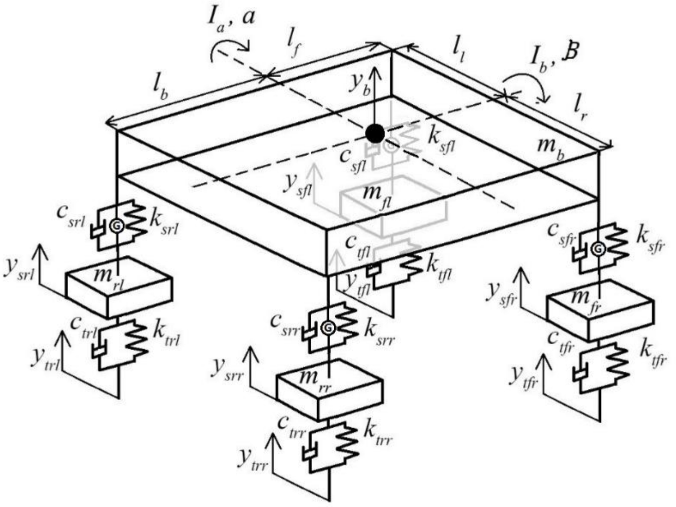

Figure 6: A full VSS model with the regenerative shock absorbers.

Compared with the half VSS model, the full VSS model has an additional rolling mode motion which makes it sensitive to the transverse road profile elevations. The full vehicle body displacement is y_b, the displacement variations of the front right, front left, rear right and rear left tires are y_{sfr}, y_{sfl}, y_{srr}, y_{srl}, respectively. The road profile displacement variation under the front right, front left, rear right and rear left are $y_{tfr}, y_{tfl}, y_{trr}, y_{trl}$, respectively. Similar to Eq. (4), the generated electric voltage balance equations of four RSAs on a full model are given by:

$$\begin{cases} L_e \cdot \dfrac{\dot{U}_{fr}}{R} + \dfrac{U_{fr}}{R} \cdot \left(R_e + R\right) = \dfrac{k_e \cdot i}{r} \cdot \left(\dot{y}_{sfr} - \dot{y}_b + l_f \cdot \dot{\alpha} + l_r \cdot \dot{\beta}\right) \\ L_e \cdot \dfrac{\dot{U}_{fl}}{R} + \dfrac{U_{fl}}{R} \cdot \left(R_e + R\right) = \dfrac{k_e \cdot i}{r} \cdot \left(\dot{y}_{sfl} - \dot{y}_b + l_f \cdot \dot{\alpha} - l_l \cdot \dot{\beta}\right) \\ L_e \cdot \dfrac{\dot{U}_{rr}}{R} + \dfrac{U_{rr}}{R} \cdot \left(R_e + R\right) = \dfrac{k_e \cdot i}{r} \cdot \left(\dot{y}_{srr} - \dot{y}_b - l_b \cdot \dot{\alpha} + l_r \cdot \dot{\beta}\right) \\ L_e \cdot \dfrac{\dot{U}_{rl}}{R} + \dfrac{U_{rl}}{R} \cdot \left(R_e + R\right) = \dfrac{k_e \cdot i}{r} \cdot \left(\dot{y}_{srl} - \dot{y}_b - l_b \cdot \dot{\alpha} - l_l \cdot \dot{\beta}\right) \end{cases} \tag{8}$$

The energy equations of the full VSS model are given in Eq. (9). Eq. (9) can be substituted back in Eq. (2) for the derivation of the equations of motion, which is shown in Appendix C.

$$\begin{cases}
T=\frac{1}{2}\cdot m_b\cdot\dot{y}_b{}^2+\frac{1}{2}\cdot m_{fr}\cdot\dot{y}_{sfr}{}^2+\frac{1}{2}\cdot m_{rr}\cdot\dot{y}_{srr}{}^2+\frac{1}{2}\cdot m_{rl}\cdot\dot{y}_{srl}{}^2+\frac{1}{2}\cdot m_{fl}\cdot\dot{y}_{sfl}{}^2+\frac{1}{2}\cdot m_s\cdot\left(\dot{y}_{sfr}-\dot{y}_b+l_f\cdot\dot{\alpha}+l_r\cdot\dot{\beta}\right)^2 \\
+\frac{1}{2}\cdot m_s\cdot\left(\dot{y}_{srr}-\dot{y}_b-l_b\cdot\dot{\alpha}+l_r\cdot\dot{\beta}\right)^2+\frac{1}{2}\cdot m_s\cdot\left(\dot{y}_{srl}-\dot{y}_b-l_b\cdot\dot{\alpha}-l_l\cdot\dot{\beta}\right)^2+\frac{1}{2}\cdot m_s\cdot\left(\dot{y}_{sfl}-\dot{y}_b+l_f\cdot\dot{\alpha}-l_l\cdot\dot{\beta}\right)^2+\frac{1}{2}\cdot I_a\dot{\alpha}^2+\frac{1}{2}\cdot I_b\dot{\beta}^2 \\
\\
W=\frac{1}{2}\cdot c_{sfr}\cdot\left(\dot{y}_{sfr}-\dot{y}_b+l_f\cdot\dot{\alpha}+l_r\cdot\dot{\beta}\right)^2+\frac{1}{2}\cdot c_{srr}\cdot\left(\dot{y}_{srr}-\dot{y}_b-l_b\cdot\dot{\alpha}+l_r\cdot\dot{\beta}\right)^2+\frac{1}{2}\cdot c_{srl}\cdot\left(\dot{y}_{srl}-\dot{y}_b-l_b\cdot\dot{\alpha}-l_l\cdot\dot{\beta}\right)^2 \\
+\frac{1}{2}\cdot c_{sfl}\cdot\left(\dot{y}_{sfl}-\dot{y}_b+l_f\cdot\dot{\alpha}-l_l\cdot\dot{\beta}\right)^2+\frac{1}{2}\cdot c_L\cdot\left(\dot{y}_{sfr}-\dot{y}_b+l_f\cdot\dot{\alpha}+l_r\cdot\dot{\beta}\right)^2+\frac{1}{2}\cdot c_L\cdot\left(\dot{y}_{srr}-\dot{y}_b-l_b\cdot\dot{\alpha}+l_r\cdot\dot{\beta}\right)^2 \\
+\frac{1}{2}\cdot c_L\cdot\left(\dot{y}_{srl}-\dot{y}_b-l_b\cdot\dot{\alpha}-l_l\cdot\dot{\beta}\right)^2+\frac{1}{2}\cdot c_L\cdot\left(\dot{y}_{sfl}-\dot{y}_b+l_f\cdot\dot{\alpha}-l_l\cdot\dot{\beta}\right)^2+\frac{1}{2}\cdot c_{tfr}\cdot\left(\dot{y}_{tfr}-\dot{y}_{sfr}\right)^2+\frac{1}{2}\cdot c_{trr}\cdot\left(\dot{y}_{trr}-\dot{y}_{srr}\right)^2 \\
+\frac{1}{2}\cdot c_{trl}\cdot\left(\dot{y}_{trl}-\dot{y}_{srl}\right)^2+\frac{1}{2}\cdot c_{tfl}\cdot\left(\dot{y}_{tfl}-\dot{y}_{sfl}\right)^2 \\
\\
V=\frac{1}{2}\cdot k_{sfr}\cdot\left(y_{sfr}-y_b+l_f\cdot\alpha+l_r\cdot\beta\right)^2+\frac{1}{2}\cdot k_{srr}\cdot\left(y_{srr}-y_b-l_b\cdot\alpha+l_r\cdot\beta\right)^2+\frac{1}{2}\cdot k_{srl}\cdot\left(y_{srl}-y_b-l_b\cdot\alpha-l_l\cdot\beta\right)^2 \\
+\frac{1}{2}\cdot k_{sfl}\cdot\left(y_{sfl}-y_b+l_f\cdot\alpha-l_l\cdot\beta\right)^2+\frac{1}{2}\cdot k_{tfr}\cdot\left(y_{tfr}-y_{sfr}\right)^2+\frac{1}{2}\cdot k_{trr}\cdot\left(y_{trr}-y_{srr}\right)^2+\frac{1}{2}\cdot k_{trl}\cdot\left(y_{trl}-y_{srl}\right)^2+\frac{1}{2}\cdot k_{tfl}\cdot\left(y_{tfl}-y_{sfl}\right)^2
\end{cases} \quad (9)$$

3. Discussions

Based on the established VSS models of the quarter, half and full in both the frequency domain and time domain, it is possible to conduct the comprehensive comparison of vibration energy harvesting and dynamic performance among these VSS models based on the realistic road profile conditions. The frequency domain analysis is conducted first to illustrate the response difference of VSS models with respect to the road excitation under one wheel. This is followed by the investigation of vehicle speed effect on the vibration energy harvesting and dynamic performance in the time domain where the accuracy of each model is discussed at different vehicle speed levels. Thirdly, the effect of shifting COG is evaluated in the frequency domain, which is then followed by the final evaluation involving real road profiles and typical driving speed cycles.

3.1 Frequency domain analysis of the vibration energy harvesting performance

The harvested power of the RSAs is analyzed in the frequency domain and compared for the different VSS models. The vibration power output transmissibility is defined as a ratio of the harvested power divided by the input excitation displacement amplitude. For the quarter VSS model, the wheel is excited in the frequency range from 0 to 25 Hz, the vibration power output transmissibility is calculated and shown in Figure 7.

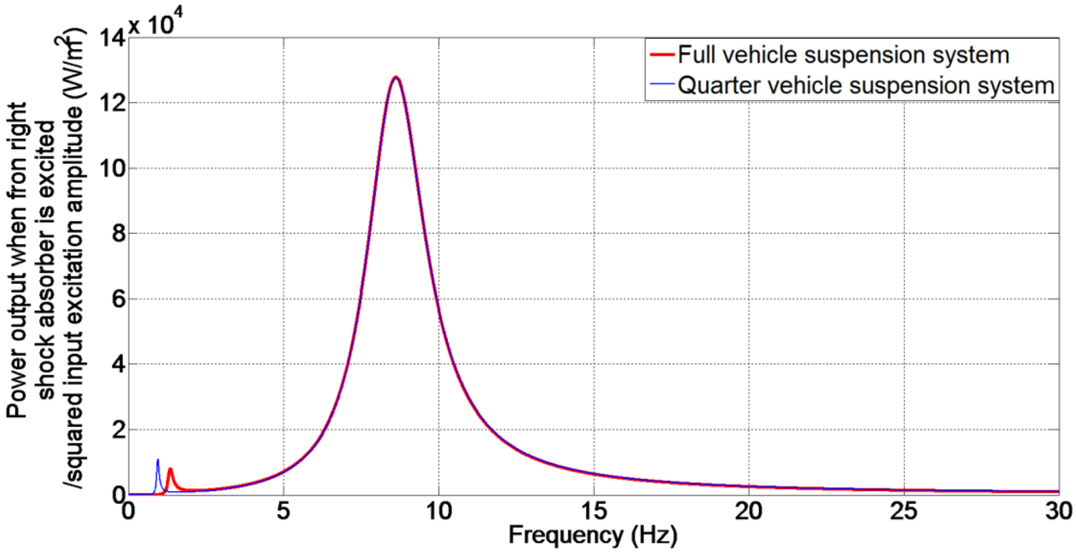

(a)

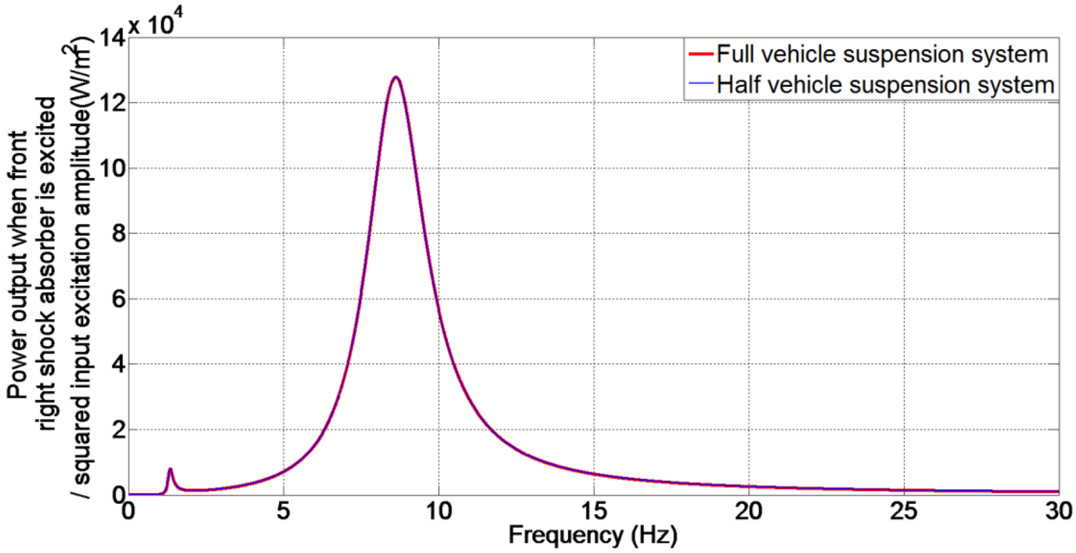

(b)

Figure 7: The ratio of total output power over squared excitation displacement amplitude of (a) full and quarter VSS models, (b) full and half VSS models.

Figure 7 compares the total harvested power output results in the same frequency range when the same excitation is applied on the only wheel in the quarter VSS model and one of two wheels in the half VSS model and one of four wheels in the full VSS model. The main output power peak occurs at 8.6 Hz which is the same as that for the quarter, half and full VSS models. In the full VSS model, the secondary output power peaks are not as obvious as that in the quarter VSS model, which occurs at 1 Hz. The interaction or coupling effects of the four quarter wheel suspension systems in the full VSS model may slightly increase the equivalent suspension stiffness of the full VSS model, which may result in a slight increase of the first peak frequency of the vibration power output transmissibility in the full VSS model. Therefore, any attempt to harvest vibration energy from the secondary peak frequencies does not generate a large power output because less amount of energy is generated at the low frequency range, as suggested by the result of the full VSS model. However some literatures studied potential of the energy harvesting at the secondary peaks using either the quarter or half VSS model, which needs to be further studied for its feasibility [19, 42].

The vibration power output transmissibility of each shock absorber on the full VSS model is shown in Figure 8. At the main peak power frequency, the most harvested power is generated from the shock absorber directly under the wheel excitation. The rest of shock absorbers have the power peaks only at the low frequency range with a magnitude much smaller than that of the excited shock absorber at 8.6 Hz. It is further indicated that the energy generated at non-peak power frequencies is much smaller than that at the peak power frequencies and is negligible. The quarter VSS model is valid around the main peak power frequency and cannot be used for the vibration energy harvesting analysis at the peak power frequencies lower than the main peak power frequency. By contrast, the half VSS model presents the results that are closer to those of the full VSS model.

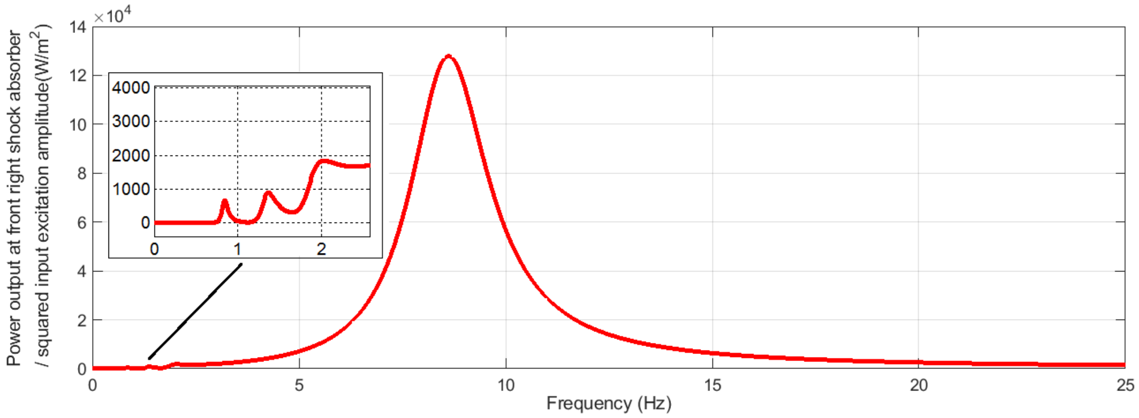

(a)

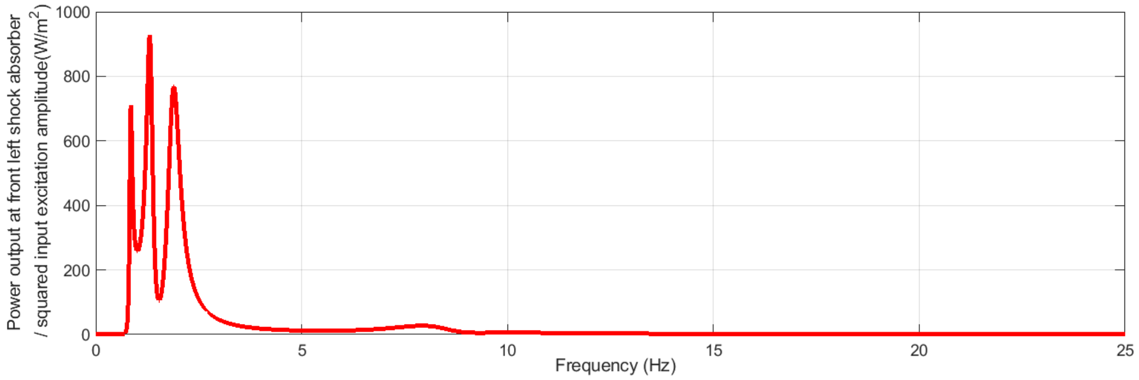

(b)

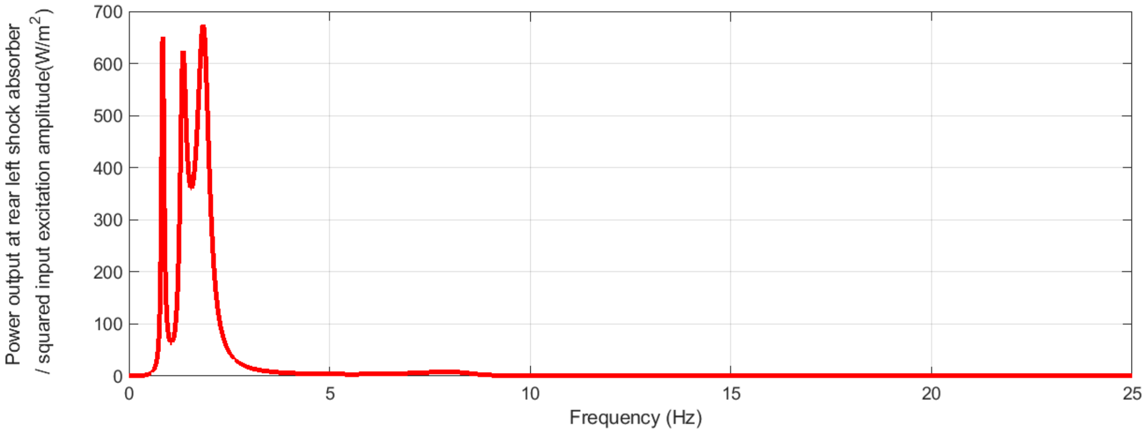

(c)

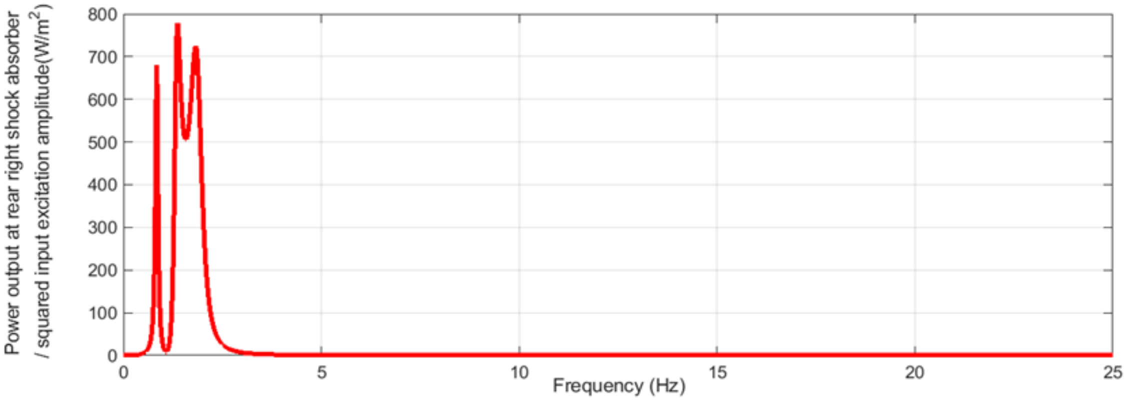

(d)

Figure 8: The ratio of output power over squared excitation displacement amplitude in the full VSS model of (a) front right regenerative shock absorber, (b) front left regenerative shock absorber, (c) rear right regenerative shock absorber, (d) rear left regenerative shock absorber when the wheel under the front right regenerative shock absorber is excited.

3.2 The effect of the vehicle speed

The vehicle speed is an important factor which influences the vibration energy harvesting performance of VSSs. In a quarter VSS model, the vehicle speed can be reflected if time trace of road profile input is given. When vehicle speed increases the input excitation frequency of the road profile will increase and the quarter VSS responds at the increased frequency accordingly. This, however, does not take into account the interaction between the front and rear wheels along the vehicle moving direction. A moving vehicle has its front and rear wheels passing the same road profile at different time, the interval of which depends on the vehicle speed. This time interval leads to a phase difference of the road input excitation signals from the front and rear wheels. This phase difference may result in a difference of the harvested power output between the quarter and full/half VSS models which needs to be investigated. The VSS models are subjected to the same sine wave road profile which has infinite length and 0.03 m displacement amplitude in the vertical direction and 1 m wavelength in the longitudinal driving direction, as shown in Figure 9. The road elevations are longitudinally applied and the transverse road profile variations are neglected.

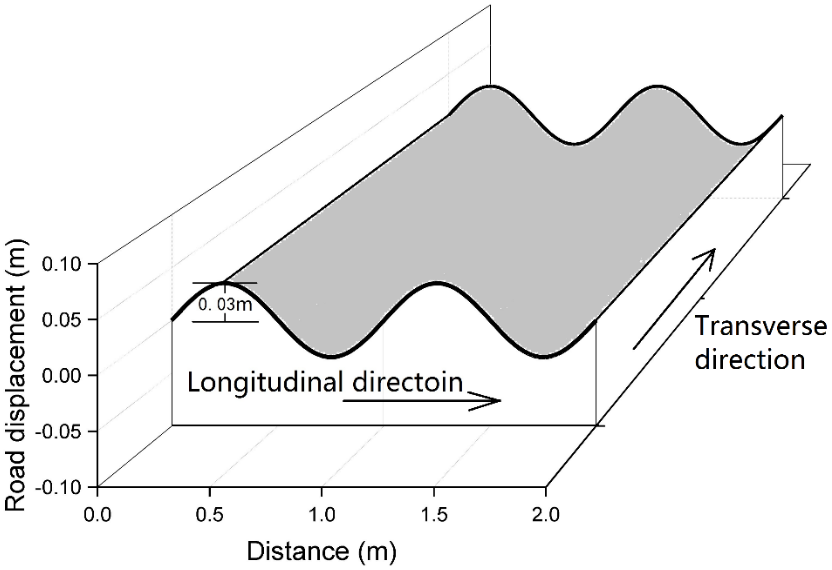

Figure 9: The sine wave road profile with the vertical elevation amplitude of 0.03 m and longitudinal wavelength of 1 m.

The quarter, half and full VSS models are individually simulated in the time domain with vehicle speed of 5 m/s, 10 m/s, 15 m/s, 20 m/s, 25 m/s and 30 m/s, respectively. The harvested power output of all the existing RSAs are summed up and averaged in the time domain to obtain the total averaged harvested power output of the vehicle against the vehicle speed, the results are shown in Figure 10.

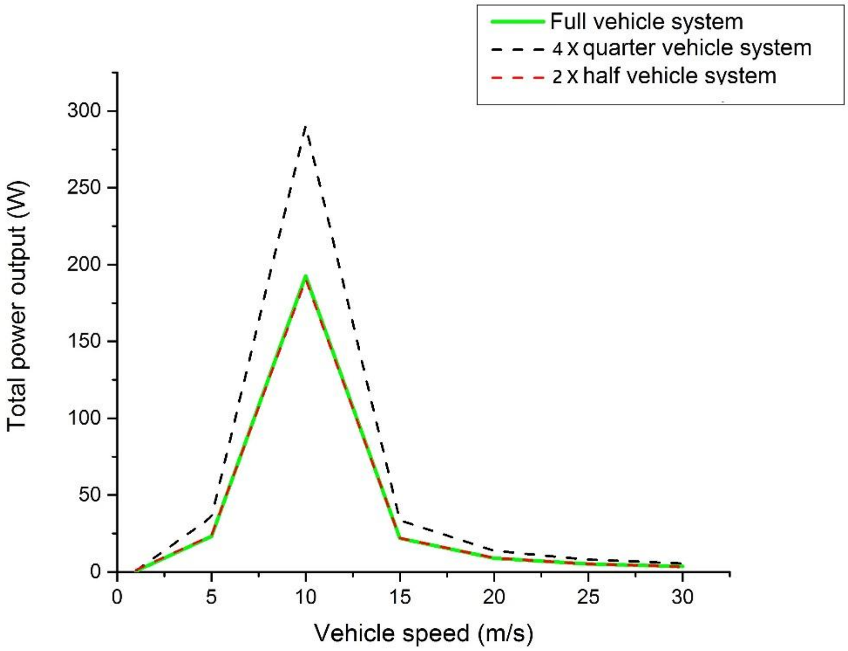

Figure 10: The total averaged harvested power output of the full, 2 times half and 4 times quarter VSS models versus the vehicle speeds of 1 m/s, 5m/s, 10 m/s,15 m/s, 20m/s, 25m/s, 30m/s.

In Figure 10, it is shown that when vehicle speed increases, the frequency of the road profile displacement excitation increases as well, resulting in a peak of the total averaged harvested power output for all the VSS models at about 10 m/s. This is because with the input road excitation displacement profile wavelength of 1 m, at the vehicle speed of 10 m/s the road excitation frequency becomes 10 Hz, which is close to the peak frequency of 8.6 Hz for the main harvested power output peak frequency as shown in Figure 7.

Since the quarter VSS model can only simulate the harvested power output of one RSA where the total harvested power output of the full VSS can be predicted by multiplying the harvested power output of the quarter VSS model by a factor of 4. Similarly, multiplying the harvested power output of the half VSS model by a factor of 2 can also predict the total harvested power output of the full VSS. It can be seen that prediction result using the half VSS model almost coincides with that of the actual full VSS model. This is because the full suspension system model is more sensitive to the rolling motion mode due to the road roughness in the transverse direction, which is not usually reflected in the given road excitation profiles. The predicted results using the quarter VSS model, however, is much higher than that of the full VSS model. The reason is that the quarter VSS model does not take into account the effect of pitching motion mode for which the half and full VSS models do. As a result, the canceling out of the harvested output power values of the front and rear RSAs is ignored. Both the half and full VSS models respond to the road elevations applied in the longitudinal directions, which induces a pitching motion mode of the vehicle. The pitching motion mode of the vehicle caused by the elevation phase difference of the front and rear wheels cannot be simulated and reflected in the quarter VSS model. Therefore, when the road transverse profile variation is negligible, which is the common case, the half VSS model presents a better simulation accuracy than the quarter VSS model regardless of the vehicle speed variation.

3.3 The effect of the vehicle center of gravity position

Shift of a vehicle center of gravity (COG) is a common design practice which influence the weight distribution of the vehicle, vehicle handling and drivability. Some vehicles are designed in such a way that their COG is not at the geometrical center of the vehicle because of the heavy powertrain or engine mass or simply trying to induce over-steering. Thus it is important to study the effect of the COG position on the vibration energy harvesting performance of the VSS models.

It is assumed here that the original VSS model has a COG located in the exact geometry center of the vehicle. When a vehicle is loaded, the COG position can be shifted in the longitudinal direction or transverse direction or both. The shifted COG position can affect the relative movement of the RSAs, the speed of which is closely related to the harvested power output. In Figure 11, the COG position of the vehicle is first shifted to the right side for 50%, then to the front side for 50% and finally to the front right corner for 50%, corresponding to the positions of a, b and c, respectively.

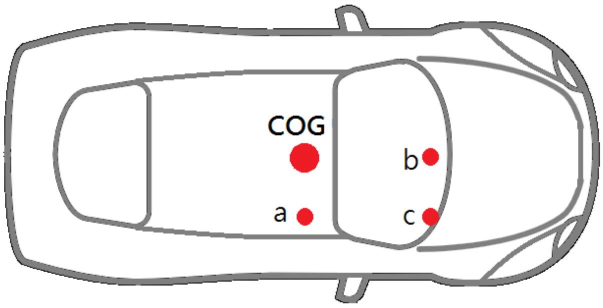

Figure 11: The top view of the positions of the center of gravity after being shifted.

Only the front right wheel is excited, and the ratio of the harvested power output of each shock absorber to the squared road excitation displacement amplitude is plotted and shown in Figure 12. In Figure 12(a), it can be seen that the RSA directly under the excitation wheel generates the most and same amount of power output at the natural frequency of 8.6 Hz for all the different COG positions. The shift of COG position does not change the trend that the power output peak amplitudes occurring at the frequencies less than 5 Hz because the RSAs not directly under the excitation wheel are significantly smaller than that at the frequency of 8.6 Hz for the RSA directly under the excitation wheel. The power out peak amplitudes of the RSAs above the front wheels are larger than those above the rear wheels. The power out peak amplitudes of the RSAs above the right wheels are larger than those above the left wheels. This is because the front right wheel is excited, the power output peak amplitudes of the RSAs close to the excitation wheel are larger than those away from the excitation wheel.

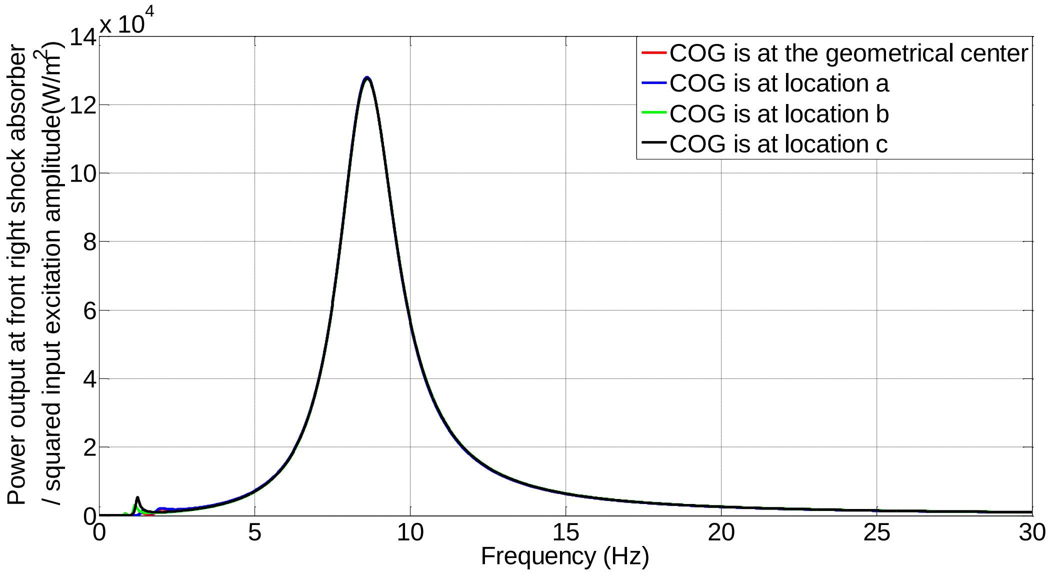

(a)

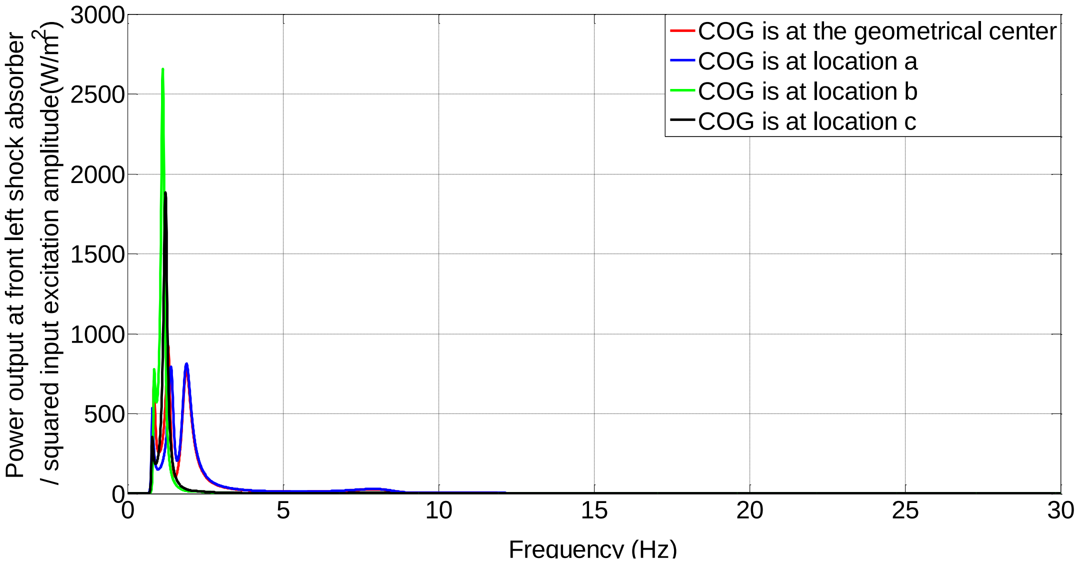
Power output at front left shock absorber / squared input excitation amplitude(W/m^2)
Frequency (Hz)
0
500
1000
1500
2000
2500
3000
0
5
10
15
20
25
30
COG is at the geometrical center
COG is at location a
COG is at location b
COG is at location c

(b)

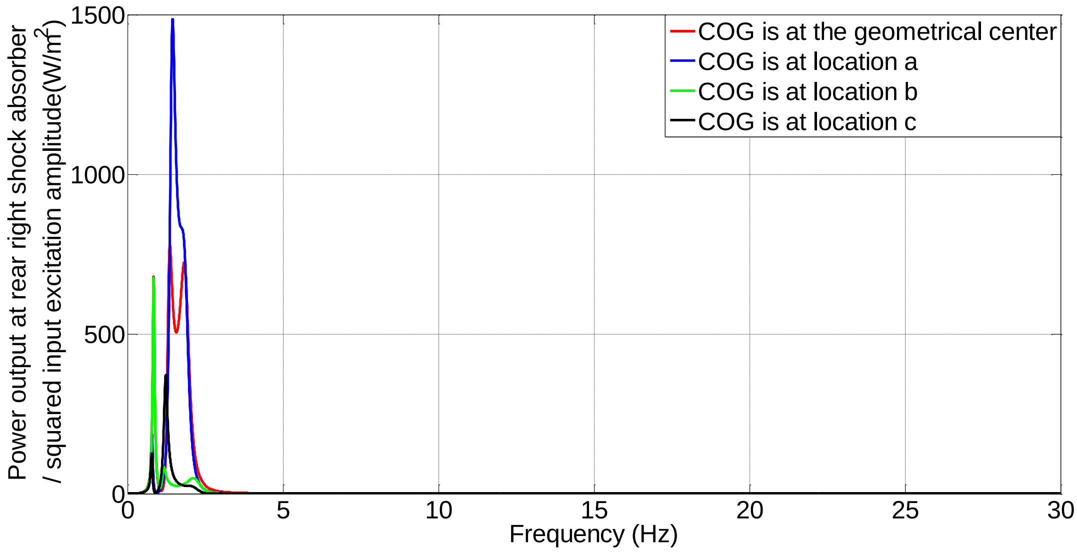
Power output at rear right shock absorber / squared input excitation amplitude(W/m^2)
Frequency (Hz)
0
500
1000
1500
0
5
10
15
20
25
30
COG is at the geometrical center
COG is at location a
COG is at location b
COG is at location c

(c)

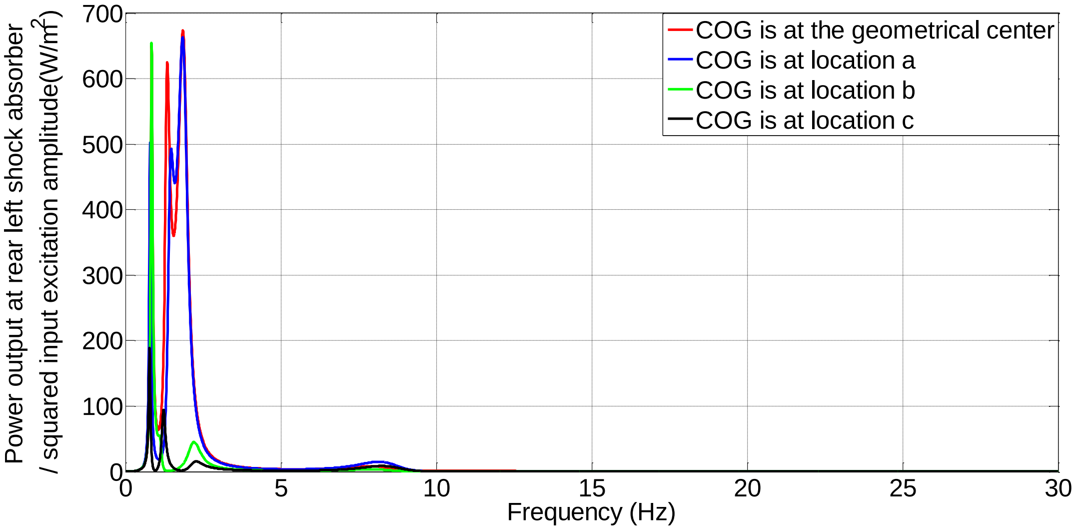

(d)

Figure 12: The ratio of output power over squared excitation displacement amplitude on the full model with the COG at the positions of a, b, c of (a) front right RSA, (b) front left RSA, (c) rear right RSA, (d) rear left RSA when the wheel under the front right RSA is excited.

In Figure 13, the ratios of the total power output of four shock absorbers to the squared road displacement excitation amplitude are calculated, presented and compared for the COG positions of a, b and c. Even though the position shift of the COG can sometimes increase the power output of the RSAs, the increased power output peak amplitudes only occur in the frequency range less than 5 Hz and are insignificant. Moreover, the excitation in the lower frequency range will generate the excessive acceleration of the vehicle cabin, which is undesirable for the ride comfort; hence resonant vibration energy harvesting in the low frequency range should be avoided. The effect of the position shift of the COG on the total harvested power output peak amplitude is also negligible at the main power output peak frequency, indicating that there is hardly any potential in improving the power generation of the RSA through changing the position of the COG. Because of the resemblance of the power output ratio curves of the quarter, half and full VSS models at the main power output peak frequency, it is safe to say that full VSS model can be represented by the quarter and half VSS models even if the COG is not located at the geometrical center of the vehicle.

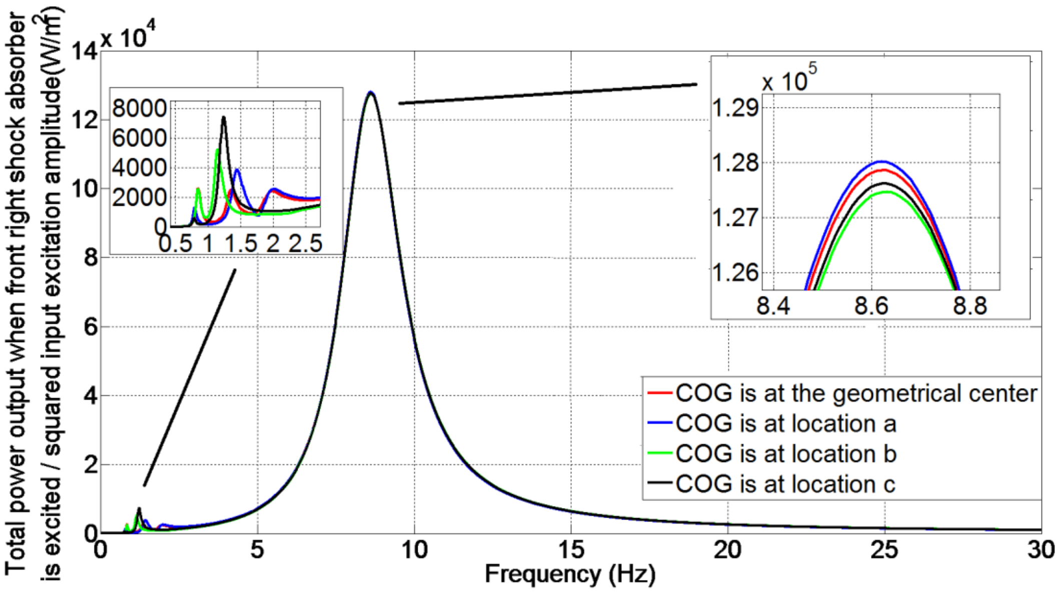

Figure 13: The ratios of the total power output of the full VSS model over the squared excitation displacement amplitude with the COG located at the positions of a, b, c.

3.4 The effects of the driving cycles and road classes

Road profiles can be categorized into different classes in terms of roughness and each class of the road profiles is expected to have different impacts on the harvested power output of the RSA. According to [18], Road classes A, C and E are presented in Figure 14. Because the road classifications associated with the vehicle speed can largely affect the power output, it would be necessary to consider the both for a full picture.

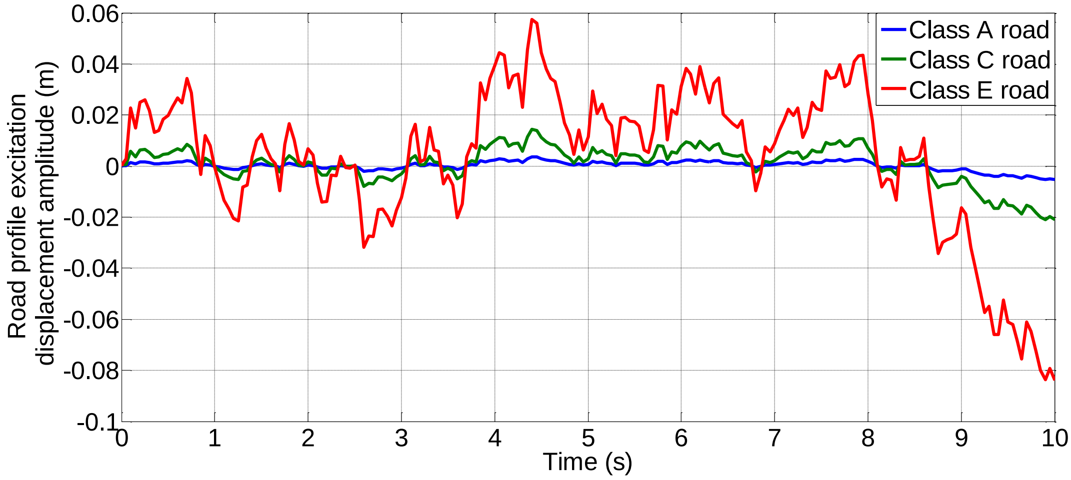

Figure 14: The modelling of the road profiles of Classes A, C and E in the time domain when the vehicle is travelling at 5.556 m/s (20 km/h).

Shown in Figure 15 are three types of driving cycles that are typical for everyday driving: NEDC (New European Driving Cycle) for European standard, HWFET (Highway Fuel Economy Test) for transient cycles and FTP-15 (Federal Test Procedure) for United States standard. The NEDC cycles are a modal driving cycle that considers the phases of constant speed and acceleration and decelerations. It resembles the combination of the urban driving at the first 800 seconds and the ultra-urban driving after 800 seconds. The HWFET cycles and FTP-75 cycles are transient driving cycles with wider speed and acceleration ranges where the HWFET cycles represent mostly highway driving and FTP-75 cycles resemble the urban driving with frequent start-stops [43]. It can be seen that for the HWFET cycles the vehicle speed maintains at about 25 m/s (90 km/h) and never drops below 1.4 m/s (50 km/h) except for the start and stop. By contrast, the NEDC and FTP-75 cycles involve more speed changes where the NEDC cycles have more stopping times and the FTP-75 cycles tend to accelerate and decelerate more frequently.

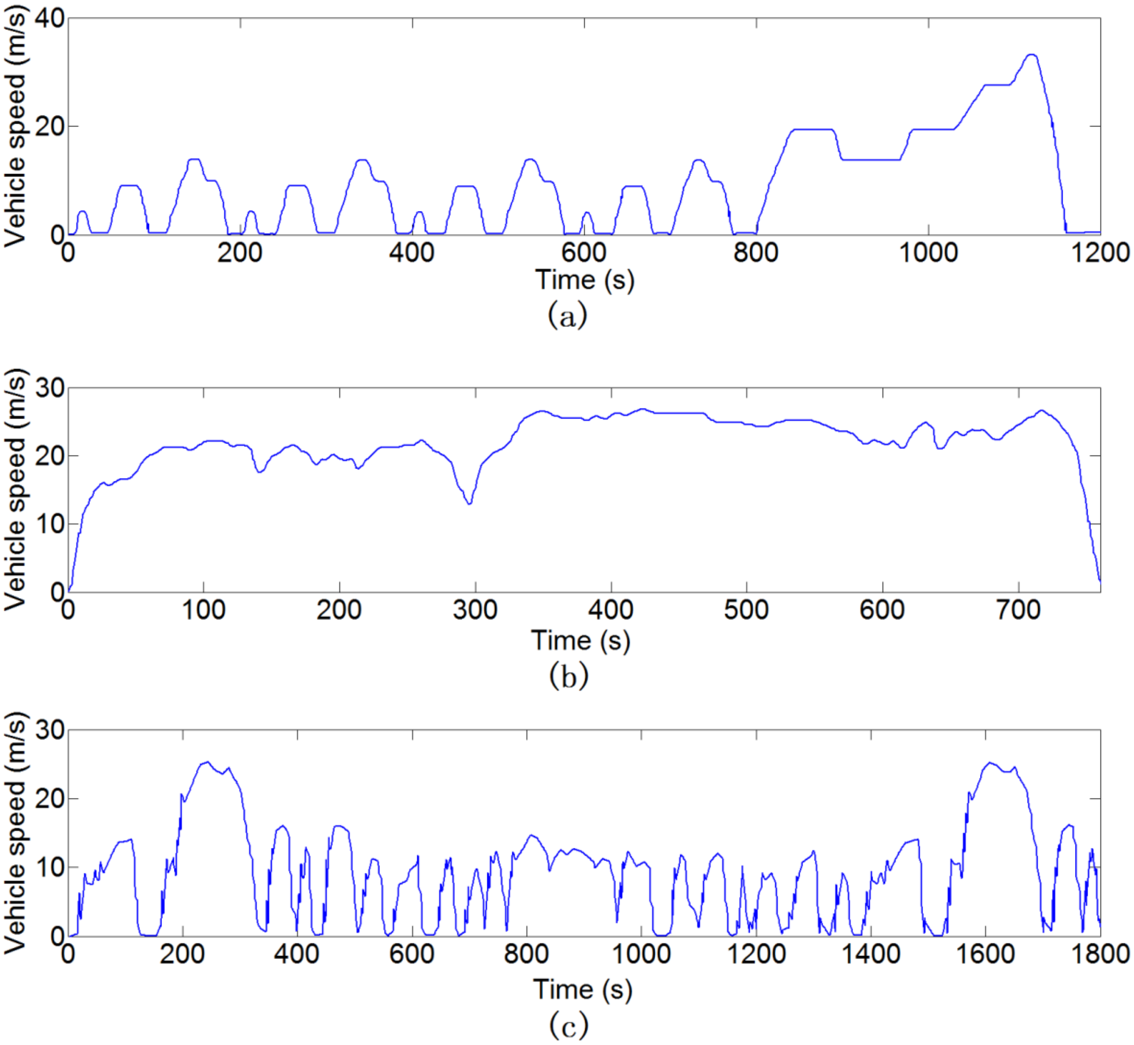

(a)

(b)

(c)

Figure 15: The vehicle speed time trace of (a) the NEDC driving cycles, (b) HWFET driving cycles and (c) FTP-75 driving cycles.

In order to examine the prediction accuracy of the harvested power output of the vehicle RSAs in a VSS in response to the realistic road conditions, the road profile of Class A, C and E combined with three driving speed cycles are applied as road excitation inputs for the VSS models of the quarter, half and full, as shown in the flow diagram in Figure 16. The time interval of the front and rear wheels passing the same road location are taken into account in the half and full VSS models. The degrees of freedom of pitching and rolling motion modes are added into the full VSS model, while the degree of freedom of pitching motion is added into the half VSS model.

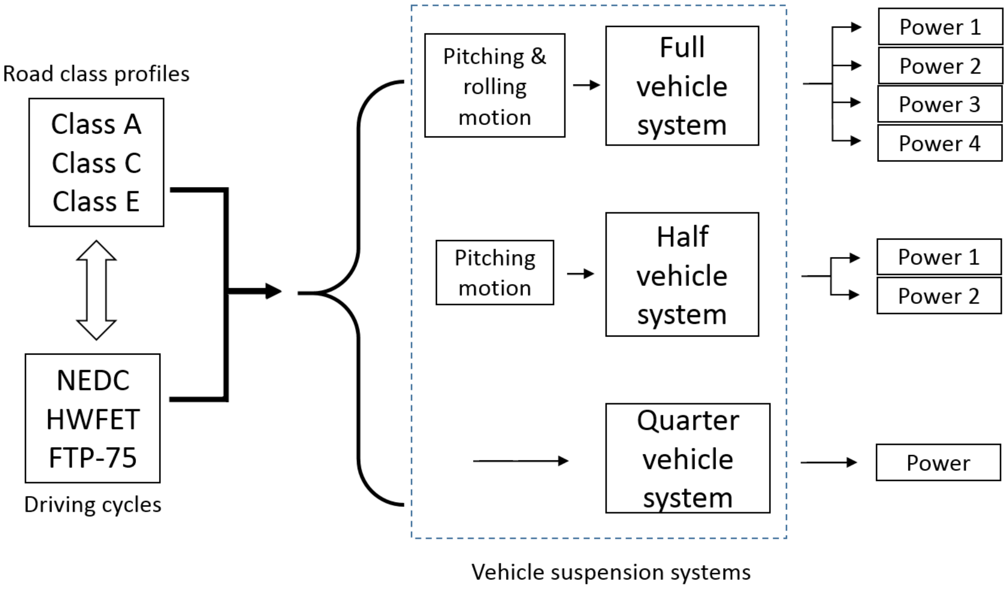

Figure 16: Evaluation process flow diagram based on different road class profiles and driving speed cycles.

Due to the random nature of the road profile, the resulting power outputs vary randomly, which makes it hard to quantify and compare the power outputs. Therefore, a 99% confidence interval is applied to the results. A confidence interval defines how much uncertainty there is for a statistic random variable under the normal distribution. In this case with the confidence internal of 99%, the power output is 99% likely to be in the calculated range for that specific road classification and driving speed cycle. Therefore it is confident to state that these power output ranges can represent actual power outputs, thus allowing for the comparison to be conducted. The comparison results are shown in Figure 17. The distance between two horizontal bars indicates the power output range with 99% confidence interval. For a fair comparison with the total averaged power outputs of the full VSS model, the total averaged power outputs of the quarter and half VSS models are multiplied by 4 and 2, respectively, to derive the comparable results of the full VSS model.

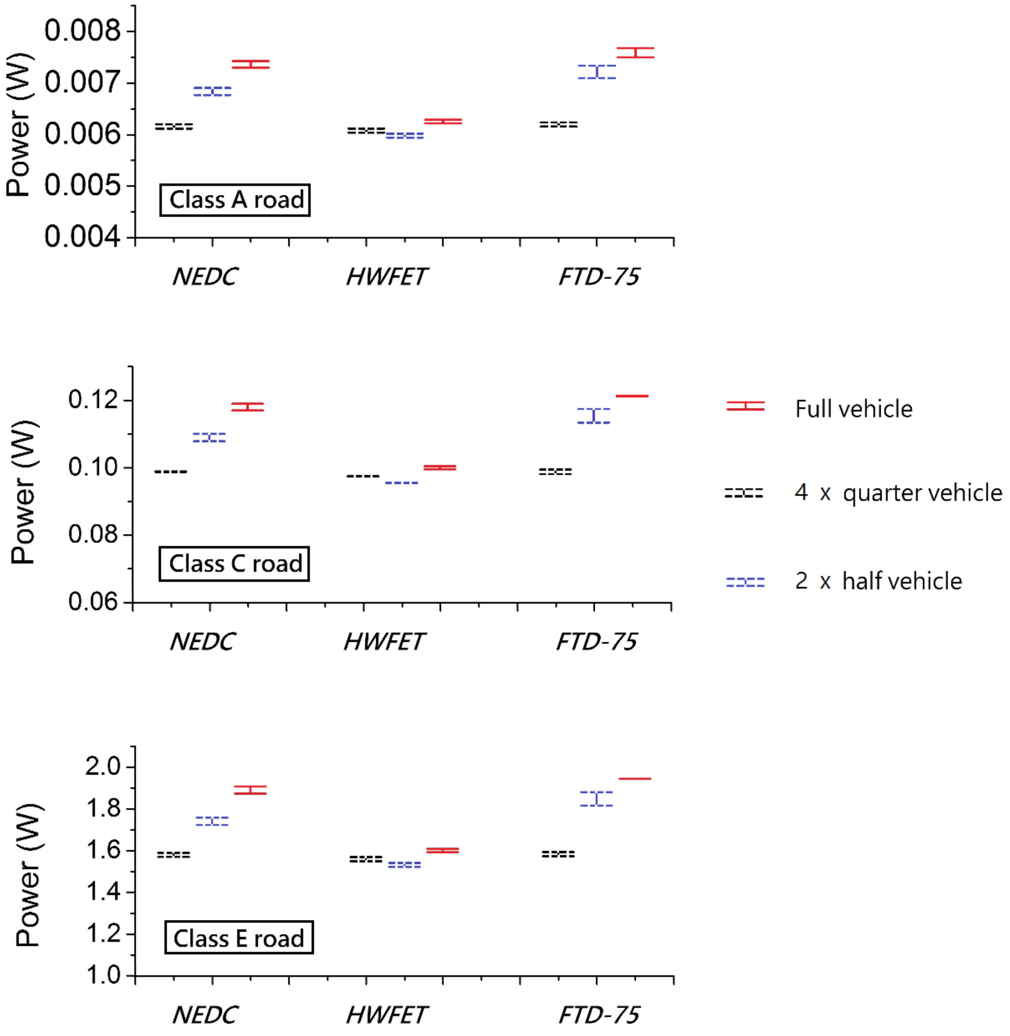

Figure 17: The comparison of the total averaged harvested power output of the full, 4 times quarter and 2 times half VSS models on Road Classes A, C and E under the driving speed cycles of the NEDC, HWFET and FTD-75.

It is shown in Figure 17 that the increase of the road classification can greatly increase the power output for all the VSS models, regardless of the driving speed cycles. With the focus on the full VSS model, for any road classification, the RSAs under the NEDC cycle and FTP-75 cycle produce similar power outputs. Both the power outputs under the NEDC cycle and FTP-75 cycle are higher than that under the HWFET cycle. This is because the HWFET cycle does not have as many speed changes as the NEDC and FTP-75 cycles. It is also supported by the fact that the RSAs under FTP-75 cycle generate slightly higher power output than that under the NEDC cycle, which is caused by more frequent accelerations and decelerations in the FTP-75 cycle. Based on the comparison of the VSS models, it is interesting to find that the quarter VSS model responds largely only to the road classifications and not largely to the driving speed cycles. The harvested power output prediction using the quarter VSS model remains the same despite of the different driving speed cycles. Additionally for all the road classifications and all the driving speed cycles except for on the HWFET cycle, the harvested power output results predicted by the half VSS model are more accurate and closer to the results of the full VSS model than those predicted by the quarter VSS model. The reason why the quarter VSS model predicts larger harvested power output than the half VSS model under the HWFET cycle is that the quarter VSS model is more likely to be excited for resonances than the half VSS model under the same HWFET cycle. It is evident in Figure 10 where the harvested power output predicted by the quarter VSS model becomes larger than that of the actual full VSS model when the VSS resonates near the main modal natural frequency.

4. Conclusion

This study was undertaken to investigate the harvested power output differences predicted by the quarter, half and full VSS models where the vibration energy is harvested from the RSAs. Three VSS models of the quarter, half and full were developed in both the frequency domain and time domain based on the same baseline vehicle. The harvested power outputs of the RSAs of each VSS model were calculated. The responses of harvested power outputs to the road excitation frequency, the effect of vehicle speed and the effect of the center of gravity position were investigated and compared for the three VSS models. Finally all the VSS models were simulated under the realistic on-road conditions under different driving speed cycles and different road classifications where the prediction accuracies of the harvested power outputs were compared, aiming to understanding how different VSS models could be utilized under the real road situations.

The research results show that most of vibration energy can be harvested at the main natural resonant frequency which is the hopping modal resonant frequency. The harvested power output of the RSAs predicted by the quarter VSS model is slightly higher at the lower frequency range; which disagrees with the result predicted by the half and full VSS models, indicating that prediction of the harvested power outputs of the RSAs through the quarter VSS model at low frequency is not feasible. The half and full VSS models present similar results where it is shown that the vehicle speed has a large effect on the harvested power output. The quarter VSS model cannot accurately predict the trend of the harvested power outputs of the RSAs with vehicle speed change. Based on the frequency domain analysis, the effect of the vehicle center of gravity position on the harvested power output only occurs in the low frequency range and is almost negligible. Therefore, when the vehicle center of gravity is not located at the geometrical center of a vehicle, the quarter and half VSS models are still as accurate as the full VSS model. In order to compare the three VSS models with realistic on-road conditions, road classifications and driving speed cycles were applied as the time domain excitation inputs for the three VSS models. The results show that driving speed cycle with more speed changes enable the RSAs to yield higher power output, such as the FTP-75 cycle, and the quarter, half and full VSS models predict the harvested power outputs of the RSAs well in terms of the road classifications. The predicted harvested power of the quarter VSS model is more sensitive to the road classifications than to the driving speed cycles. Therefore in general with transverse road profile variations being neglected, the half VSS model is a good candidate for predicting the harvested power output in place of the full VSS model when the driving speed variations are considered. The quarter VSS model only maintains its prediction accuracy where the vehicle speed variations is not large such as when the vehicle is being driven on the highway.

Reference

1. Zhang, R., et al., *The effects of the electro-mechanical coupling and Halbach magnet pattern on energy*

harvesting performance of a two degree of freedom electromagnetic vibration energy harvester. International Journal of Vehicle Noise and Vibration, 2018. **14**(2): p. 124-146.

2. Zhang, X. and C. Mi, *Vehicle power management: basic concepts*, in *Vehicle Power Management*. 2011, Springer. p. 13-48.
3. Zhang, R., X. Wang, and S. John, *A comprehensive review of the techniques on regenerative shock absorber systems.* Energies, 2018. **11**(5): p. 1167.
4. Zhang, R., X. Wang, and Z. Liu, *A novel regenerative shock absorber with a speed doubling mechanism and its Monte Carlo simulation*. Journal of Sound and Vibration, 2018. **417**: p. 260-276.
5. Zuo, L., et al., *Design and characterization of an electromagnetic energy harvester for vehicle suspensions.* Smart Materials and Structures, 2010. **19**(4): p. 045003.
6. Xie, X. and Q. Wang, *Energy harvesting from a vehicle suspension system.* Energy, 2015. **86**: p. 385-392.
7. Gupta, A., et al., *Design of electromagnetic shock absorbers.* International Journal of Mechanics and Materials in Design, 2006. **3**(3): p. 285-291.
8. Zhang, P.S., *Design of Electromagnetic Shock Absorbers for Energy Harvesting From Vehicle Suspensions*. 2010, MS thesis, Stony Brook University, Stony Brook, NY.
9. Long, Z., G. He, and S. Xue, *Study of EDS & EMS hybrid suspension system with permanent-magnet halbach array.* IEEE transactions on magnetics, 2011. **47**(12): p. 4717-4724.
10. Goldner, R., P. Zerigian, and J. Hull, *A preliminary study of energy recovery in vehicles by using regenerative magnetic shock absorbers*. 2001, SAE Technical Paper.
11. Fang, Z., et al., *Experimental study of damping and energy regeneration characteristics of a hydraulic electromagnetic shock absorber.* Advances in Mechanical Engineering, 2013. **5**: p. 943528.
12. Wang, R., et al., *Modelling, testing and analysis of a regenerative hydraulic shock absorber system.* Energies, 2016. **9**(5): p. 386.
13. Galluzzi, R., et al., *Regenerative Shock Absorbers and the Role of the Motion Rectifier*. 2016, SAE Technical Paper.
14. Li, Z., et al. *A motion rectifier based energy harvesting shock absorbers*. in *2012 ASME Design Engineering Conference, Chicago, Aug12-15*. 2012.
15. Li, P. and L. Zuo, *Assessment of vehicle performances with energy-harvesting shock absorbers.* SAE International Journal of Passenger Cars-Mechanical Systems, 2013. **6**(2013-01-0170): p. 18-27.
16. Salman, W., et al., *A high-efficiency energy regenerative shock absorber using helical gears for powering low-wattage electrical device of electric vehicles.* Energy, 2018. **159**: p. 361-372.
17. Guo, S., et al., *Performance evaluation and parameter sensitivity of energy-harvesting shock absorbers on different vehicles.* Vehicle System Dynamics, 2016. **54**(7): p. 918-942.
18. Zhang, R. and X. Wang, *Parameter study and optimization of a half-vehicle suspension system model integrated with an arm-teeth regenerative shock absorber using Taguchi method.* Mechanical Systems and Signal Processing, 2019. **126**: p. 65-81.
19. Zhang, R., et al., *A novel indirect-drive regenerative shock absorber for energy harvesting and comparison with a conventional direct-drive regenerative shock absorber.* Applied Energy, 2018. **229**: p. 111-127.
20. Fukumori, Y., et al., *Study on Independent Tuning Damping Characteristic by Coupling of Electromagnetic Dampers for Automobiles*. 2015, SAE Technical Paper.
21. Zheng, X.-c., F. Yu, and Y.-c. Zhang, *A novel energy-regenerative active suspension for vehicles*. Journal of Shanghai Jiaotong University (Science), 2008. **13**(2): p. 184-188.
22. Kawamoto, Y., et al., *Modeling of electromagnetic damper for automobile suspension.* Journal of System

Design and Dynamics, 2007. **1**(3): p. 524-535.

23. Kawamoto, Y., et al., *Electro-mechanical suspension system considering energy consumption and vehicle manoeuvre*. Vehicle System Dynamics, 2008. **46**(S1): p. 1053-1063.
24. Zhang, Y., et al. *Experimental verification of energy-regenerative feasibility for an automotive electrical suspension system*. in *Vehicular Electronics and Safety, 2007. ICVES. IEEE International Conference on*. 2007. IEEE.
25. Liu, Y., L. Xu, and L. Zuo, *Design, Modeling, Lab and Field Tests of a Mechanical-motion-rectifier-based Energy Harvester Using a Ball-screw Mechanism*. IEEE/ASME Transactions on Mechatronics, 2017.
26. Xie, L., et al., *Damping-tunable energy-harvesting vehicle damper with multiple controlled generators: Design, modeling and experiments*. Mechanical Systems and Signal Processing, 2018. **99**: p. 859-872.
27. Demetgul, M. and I. Guney, *Design of the Hybrid Regenerative Shock Absorber and Energy Harvesting from Linear Movement*. Journal of Clean Energy Technologies, 2017. **5**(1).
28. Cho, T., et al. *Design, development and evaluation of an energy-harvesting electromagnetic shock absorber*. in *Proceedings of the 14th IFToMM World Congress*. 2015. 國立臺灣大學機械系.
29. Liu, Y., et al., *Energy-Regenerative Shock Absorber for Transportation Vehicles Based on Dual Overrunning Clutches: Design, Modeling, and Simulation*. Transportation Research Record: Journal of the Transportation Research Board, 2016(2551): p. 126-136.
30. Singh, S. and N.V. Satpute, *Design and analysis of energy-harvesting shock absorber with electromagnetic and fluid damping*. Journal of Mechanical Science and Technology, 2015. **29**(4): p. 1591.
31. Choi, S., M. Seong, and K. Kim, *Vibration control of an electrorheological fluid-based suspension system with an energy regenerative mechanism*. Proceedings of the Institution of Mechanical Engineers, Part D: Journal of Automobile Engineering, 2009. **223**(4): p. 459-469.
32. Lin, X., et al. *Simulation and performance evaluation of hydraulic transmission electromagnetic energy-regenerative active suspension*. in *2010 Second WRI Global Congress on Intelligent Systems*. 2010. IEEE.
33. Ding, R., et al., *Study on coordinated control of the energy regeneration and the vibration isolation in a hybrid electromagnetic suspension*. Proceedings of the Institution of Mechanical Engineers, Part D: Journal of Automobile Engineering, 2016: p. 0954407016675812.
34. Xie, L., J. Li, and M. Cai. *Design of a hybrid energy-harvesting shock absorber*. in *2015 International Forum on Energy, Environment Science and Materials*. 2015. Atlantis Press.
35. Smith, M.C. and S.J. Swift, *Power dissipation in automotive suspensions*. Vehicle System Dynamics, 2011. **49**(1-2): p. 59-74.
36. Nakano, K., *Combined type self-powered active vibration control of truck cabins*. Vehicle System Dynamics, 2004. **41**(6): p. 449-473.
37. Wei, C. and H. Taghavifar, *A novel approach to energy harvesting from vehicle suspension system: Half-vehicle model*. Energy, 2017. **134**: p. 279-288.
38. Abdelkareem, M.A., et al., *Energy harvesting sensitivity analysis and assessment of the potential power and full car dynamics for different road modes*. Mechanical Systems and Signal Processing, 2018. **110**: p. 307-332.
39. Aldair, A.A. and W.J. Wang, *The energy regeneration of Electromagnetic energy saving active Suspension in full vehicle with Neurofuzzy controller*. International Journal of Artificial Intelligence & Applications, 2011. **2**(2): p. 32-43.
40. Faheem, A., F. Alam, and V. Thomas. *The suspension dynamic analysis for a quarter car model and half car model*. in *3rd BSME-ASME international conference on thermal engineering*. 2006.

41. Al-Yafeai, D., T. Darabseh, and A.-H.I. Mourad. *Quarter vs. Half Car Model Energy Harvesting Systems*. in *2019 Advances in Science and Engineering Technology International Conferences (ASET)*. 2019. IEEE.

42. Xiao, H., X. Wang, and S. John, *A dimensionless analysis of a 2DOF piezoelectric vibration energy harvester*. Mechanical Systems and Signal Processing, 2015. **58**: p. 355-375.

43. Davari, M.M., J. Jerrelind, and A.S. Trigell, *Energy efficiency analyses of a vehicle in modal and transient driving cycles including longitudinal and vertical dynamics*. Transportation Research Part D: Transport and Environment, 2017. **53**: p. 263-275.

Appendix A. Equations of motion of the quarter vehicle suspension system model

$$\left\{\begin{array}{c} m_s\cdot\left(\ddot{x}_1-\ddot{x}_2\right)+m_1\ddot{x}_1+c_1\cdot\left(\dot{x}_1-\dot{y}\right)+c_2\cdot\left(\dot{x}_1-\dot{x}_2\right)+c_L\cdot\left(\dot{x}_1-\dot{x}_2\right) \\ +k_1\cdot\left(x_1-y\right)+k_2\cdot\left(x_1-x_2\right)+Bl\cdot\frac{U}{R_e}\cdot\frac{i\cdot r_g}{r}=0 \\ m_s\cdot\left(\ddot{x}_2-\ddot{x}_1\right)+m\cdot\ddot{x}_2+c_2\cdot\left(\dot{x}_2-\dot{x}_1\right)+c_L\cdot\left(\dot{x}_2-\dot{x}_1\right)+k_2\cdot\left(x_2-x_1\right)-Bl\cdot\frac{U}{R_e}\cdot\frac{i\cdot r_g}{r}=0 \\ L_e\cdot\frac{\dot{U}}{R_e}+\frac{U}{R_e}\cdot\left(R+R_e\right)=\frac{k_e\cdot i}{r}\cdot\left(x_1-x_2\right) \end{array}\right.$$

Appendix B. Equations of motion of the half vehicle suspension system model

$$\left\{\begin{array}{l} m_s\left(\ddot{x}_f-\ddot{x}+l_f\ddot{\theta}\right)+m_{1f}\ddot{x}_f-c_{1f}\left(\dot{z}_f-\dot{x}_f\right)+c_{2f}\left(\dot{x}_f-\dot{x}+l_f\dot{\theta}\right)+c_L\left(\dot{x}_f-\dot{x}+l_f\dot{\theta}\right)-k_{1f}\left(z_f-x_f\right)+k_{2f}\left(x_f-x+l_f\theta\right)-Bl\cdot\frac{U_f}{R}\cdot\frac{j\cdot r_g}{r}=0 \\ m_s\left(\ddot{x}_r-\ddot{x}-l_b\ddot{\theta}\right)+m_{1r}\ddot{x}_r-c_{1r}\left(\dot{z}_r-\dot{x}_r\right)+c_{2r}\left(\dot{x}_r-\dot{x}-l_b\dot{\theta}\right)+c_L\left(\dot{x}_r-\dot{x}-l_b\dot{\theta}\right)-k_{1r}\left(z_r-x_r\right)+k_{2r}\left(x_r-x-l_b\theta\right)-Bl\cdot\frac{U_r}{R}\cdot\frac{j\cdot r_g}{r}=0 \\ -m_s\left(\ddot{x}_f-\ddot{x}+l_f\ddot{\theta}\right)-m_s\left(\ddot{x}_r-\ddot{x}-l_b\ddot{\theta}\right)+m_2\ddot{x}-c_{2f}\left(\dot{x}_f-\dot{x}+l_f\dot{\theta}\right)-c_{2r}\left(\dot{x}_r-\dot{x}-l_b\dot{\theta}\right)-c_L\left(\dot{x}_f-\dot{x}+l_f\dot{\theta}\right)-c_L\left(\dot{x}_r-\dot{x}-l_b\dot{\theta}\right)-k_{2f}\left(x_f-x+l_f\theta\right) \\ -k_{2r}\left(x_r-x-l_b\theta\right)+Bl\cdot\frac{U_f}{R}\cdot\frac{j\cdot r_g}{r}+Bl\cdot\frac{U_r}{R}\cdot\frac{j\cdot r_g}{r}=0 \\ a\cdot m_s\left(\ddot{x}_f-\ddot{x}+l_f\ddot{\theta}\right)-b\cdot m_s\left(\ddot{x}_r-\ddot{x}-l_b\ddot{\theta}\right)+J\ddot{\theta}+a\cdot c_{2f}\left(\dot{x}_f-\dot{x}+l_f\dot{\theta}\right)-b\cdot c_{2r}\left(\dot{x}_r-\dot{x}-l_b\dot{\theta}\right)+a\cdot c_L\left(\dot{x}_f-\dot{x}+l_f\dot{\theta}\right)-b\cdot c_L\left(\dot{x}_r-\dot{x}-l_b\dot{\theta}\right) \\ +a\cdot k_{2f}\left(x_f-x+l_f\theta\right)-b\cdot k_{2r}\left(x_r-x-l_b\theta\right)-a\cdot Bl\cdot\frac{U_f}{R}\cdot\frac{j\cdot r_g}{r}+b\cdot Bl\cdot\frac{U_r}{R}\cdot\frac{j\cdot r_g}{r}=0 \\ L_e\cdot\frac{\dot{U}_f}{R}+\frac{U_f}{R}\cdot\left(R+R_e\right)=\frac{k_e\cdot j}{r}\cdot\left(\dot{x}_f-\dot{x}+l_f\dot{\theta}\right) \\ L_e\cdot\frac{\dot{U}_r}{R}+\frac{U_r}{R}\cdot\left(R+R_e\right)=\frac{k_e\cdot j}{r}\cdot\left(\dot{x}_r-\dot{x}-l_b\dot{\theta}\right) \end{array}\right.$$

Appendix C. Equations of motion of the full vehicle suspension system model

$$
\left\{
\begin{array}{l}
m_b\ddot{y}_b-m_s\cdot\left(\ddot{y}_{sfr}-\ddot{y}_b+l_f\cdot\ddot{\alpha}+l_r\cdot\ddot{\beta}\right)-m_s\cdot\left(\ddot{y}_{srr}-\ddot{y}_b-l_b\cdot\ddot{\alpha}+l_r\cdot\ddot{\beta}\right)-m_s\cdot\left(\ddot{y}_{srl}-\ddot{y}_b-l_b\cdot\ddot{\alpha}-l_l\cdot\ddot{\beta}\right)-m_s\cdot\left(\ddot{y}_{sfl}-\ddot{y}_b+l_f\cdot\ddot{\alpha}-l_l\cdot\ddot{\beta}\right)\\
-c_{sfr}\cdot\left(\dot{y}_{sfr}-\dot{y}_b+l_f\cdot\dot{\alpha}+l_r\cdot\dot{\beta}\right)-c_{srr}\cdot\left(\dot{y}_{srr}-\dot{y}_b-l_b\cdot\dot{\alpha}+l_r\cdot\dot{\beta}\right)-c_{srl}\cdot\left(\dot{y}_{srl}-\dot{y}_b-l_b\cdot\dot{\alpha}-l_l\cdot\dot{\beta}\right)-c_{sfl}\cdot\left(\dot{y}_{sfl}-\dot{y}_b+l_f\cdot\dot{\alpha}-l_l\cdot\dot{\beta}\right)\\
-c_L\cdot\left(\dot{y}_{sfr}-\dot{y}_b+l_f\cdot\dot{\alpha}+l_r\cdot\dot{\beta}\right)-c_L\cdot\left(\dot{y}_{srr}-\dot{y}_b-l_b\cdot\dot{\alpha}+l_r\cdot\dot{\beta}\right)-c_L\cdot\left(\dot{y}_{srl}-\dot{y}_b-l_b\cdot\dot{\alpha}-l_l\cdot\dot{\beta}\right)-c_L\cdot\left(\dot{y}_{sfl}-\dot{y}_b+l_f\cdot\dot{\alpha}-l_l\cdot\dot{\beta}\right)\\
-k_{sfr}\cdot\left(y_{sfr}-y_b+l_f\cdot\alpha+l_r\cdot\beta\right)-k_{srr}\cdot\left(y_{srr}-y_b-l_b\cdot\alpha+l_r\cdot\beta\right)-k_{srl}\cdot\left(y_{srl}-y_b-l_b\cdot\alpha-l_l\cdot\beta\right)-k_{sfl}\cdot\left(y_{sfl}-y_b+l_f\cdot\alpha-l_l\cdot\beta\right)\\
+Bl\cdot\frac{U_{fr}}{R}\cdot\frac{i\cdot r_g}{r}+Bl\cdot\frac{U_{fl}}{R}\cdot\frac{i\cdot r_g}{r}+Bl\cdot\frac{U_{rr}}{R}\cdot\frac{i\cdot r_g}{r}+Bl\cdot\frac{U_{rl}}{R}\cdot\frac{i\cdot r_g}{r}=0\\
\\
m_{fr}\cdot\ddot{y}_{sfr}+m_s\cdot\left(\ddot{y}_{sfr}-\ddot{y}_b+l_f\cdot\ddot{\alpha}+l_r\cdot\ddot{\beta}\right)+c_{sfr}\cdot\left(\dot{y}_{sfr}-\dot{y}_b+l_f\cdot\dot{\alpha}+l_r\cdot\dot{\beta}\right)+c_L\cdot\left(\dot{y}_{sfr}-\dot{y}_b+l_f\cdot\dot{\alpha}+l_r\cdot\dot{\beta}\right)+k_{sfr}\cdot\left(y_{sfr}-y_b+l_f\cdot\alpha+l_r\cdot\beta\right)\\
-c_{tfr}\cdot\left(\dot{y}_{tfr}-\dot{y}_{sfr}\right)-k_{tfr}\cdot\left(y_{tfr}-y_{sfr}\right)-Bl\cdot\frac{U_{fr}}{R}\cdot\frac{i\cdot r_g}{r}=0\\
\\
m_{rr}\cdot\ddot{y}_{srr}+m_s\cdot\left(\ddot{y}_{srr}-\ddot{y}_b-l_b\cdot\ddot{\alpha}+l_r\cdot\ddot{\beta}\right)+c_{srr}\cdot\left(\dot{y}_{srr}-\dot{y}_b-l_b\cdot\dot{\alpha}+l_r\cdot\dot{\beta}\right)+c_L\cdot\left(\dot{y}_{srr}-\dot{y}_b-l_b\cdot\dot{\alpha}+l_r\cdot\dot{\beta}\right)+k_{srr}\cdot\left(y_{srr}-y_b-l_b\cdot\alpha+l_r\cdot\beta\right)\\
-c_{trr}\cdot\left(\dot{y}_{trr}-\dot{y}_{srr}\right)-k_{trr}\cdot\left(y_{trr}-y_{srr}\right)-Bl\cdot\frac{U_{rr}}{R}\cdot\frac{i\cdot r_g}{r}=0\\
\\
m_{rl}\cdot\ddot{y}_{srl}+m_s\cdot\left(\ddot{y}_{srl}-\ddot{y}_b-l_b\cdot\ddot{\alpha}-l_l\cdot\ddot{\beta}\right)+c_{srl}\cdot\left(\dot{y}_{srl}-\dot{y}_b-l_b\cdot\dot{\alpha}-l_l\cdot\dot{\beta}\right)+c_L\cdot\left(\dot{y}_{srl}-\dot{y}_b-l_b\cdot\dot{\alpha}-l_l\cdot\dot{\beta}\right)+k_{srl}\cdot\left(y_{srl}-y_b-l_b\cdot\alpha-l_l\cdot\beta\right)\\
-c_{trl}\cdot\left(\dot{y}_{trl}-\dot{y}_{srl}\right)-k_{trl}\cdot\left(y_{trl}-y_{srl}\right)-Bl\cdot\frac{U_{rl}}{R}\cdot\frac{i\cdot r_g}{r}=0\\
\\
m_{fl}\cdot\ddot{y}_{sfl}+m_s\cdot\left(\ddot{y}_{sfl}-\ddot{y}_b+l_f\cdot\ddot{\alpha}-l_l\cdot\ddot{\beta}\right)+c_{sfl}\cdot\left(\dot{y}_{sfl}-\dot{y}_b+l_f\cdot\dot{\alpha}-l_l\cdot\dot{\beta}\right)+c_L\cdot\left(\dot{y}_{sfl}-\dot{y}_b+l_f\cdot\dot{\alpha}-l_l\cdot\dot{\beta}\right)+k_{sfl}\cdot\left(y_{sfl}-y_b+l_f\cdot\alpha-l_l\cdot\beta\right)\\
-c_{tfl}\cdot\left(\dot{y}_{tfl}-\dot{y}_{sfl}\right)-k_{tfl}\cdot\left(y_{tfl}-y_{sfl}\right)-Bl\cdot\frac{U_{fl}}{R}\cdot\frac{i\cdot r_g}{r}=0\\
\\
l_f\cdot m_s\cdot\left(\ddot{y}_{sfr}-\ddot{y}_b+l_f\cdot\ddot{\alpha}+l_r\cdot\ddot{\beta}\right)-l_b\cdot m_s\cdot\left(\ddot{y}_{srr}-\ddot{y}_b-l_b\cdot\ddot{\alpha}+l_r\cdot\ddot{\beta}\right)-l_b\cdot m_s\cdot\left(\ddot{y}_{srl}-\ddot{y}_b-l_b\cdot\ddot{\alpha}-l_l\cdot\ddot{\beta}\right)+l_f\cdot m_s\cdot\left(\ddot{y}_{sfl}-\ddot{y}_b+l_f\cdot\ddot{\alpha}-l_l\cdot\ddot{\beta}\right)+I_a\cdot\ddot{\alpha}\\
+l_f\cdot c_{sfr}\cdot\left(\dot{y}_{sfr}-\dot{y}_b+l_f\cdot\dot{\alpha}+l_r\cdot\dot{\beta}\right)-l_b\cdot c_{srr}\cdot\left(\dot{y}_{srr}-\dot{y}_b-l_b\cdot\dot{\alpha}+l_r\cdot\dot{\beta}\right)-l_b\cdot c_{srl}\cdot\left(\dot{y}_{srl}-\dot{y}_b-l_b\cdot\dot{\alpha}-l_l\cdot\dot{\beta}\right)+l_f\cdot c_{sfl}\cdot\left(\dot{y}_{sfl}-\dot{y}_b+l_f\cdot\dot{\alpha}-l_l\cdot\dot{\beta}\right)\\
+l_f\cdot c_L\cdot\left(\dot{y}_{sfr}-\dot{y}_b+l_f\cdot\dot{\alpha}+l_r\cdot\dot{\beta}\right)-l_b\cdot c_L\cdot\left(\dot{y}_{srr}-\dot{y}_b-l_b\cdot\dot{\alpha}+l_r\cdot\dot{\beta}\right)-l_b\cdot c_L\cdot\left(\dot{y}_{srl}-\dot{y}_b-l_b\cdot\dot{\alpha}-l_l\cdot\dot{\beta}\right)+l_f\cdot c_L\cdot\left(\dot{y}_{sfl}-\dot{y}_b+l_f\cdot\dot{\alpha}-l_l\cdot\dot{\beta}\right)\\
+l_f\cdot k_{sfr}\cdot\left(y_{sfr}-y_b+l_f\cdot\alpha+l_r\cdot\beta\right)-l_b\cdot k_{srr}\cdot\left(y_{srr}-y_b-l_b\cdot\alpha+l_r\cdot\beta\right)-l_b\cdot k_{srl}\cdot\left(y_{srl}-y_b-l_b\cdot\alpha-l_l\cdot\beta\right)+l_f\cdot k_{sfl}\cdot\left(y_{sfl}-y_b+l_f\cdot\alpha-l_l\cdot\beta\right)\\
+l_b\cdot Bl\cdot\frac{U_{rl}}{R}\cdot\frac{i\cdot r_g}{r}+l_b\cdot Bl\cdot\frac{U_{rr}}{R}\cdot\frac{i\cdot r_g}{r}-l_f\cdot Bl\cdot\frac{U_{fr}}{R}\cdot\frac{i\cdot r_g}{r}-l_f\cdot Bl\cdot\frac{U_{fl}}{R}\cdot\frac{i\cdot r_g}{r}=0\\
\\
l_l\cdot m_s\cdot\left(\ddot{y}_{sfr}-\ddot{y}_b+l_f\cdot\ddot{\alpha}+l_r\cdot\ddot{\beta}\right)+l_r\cdot m_s\cdot\left(\ddot{y}_{srr}-\ddot{y}_b-l_b\cdot\ddot{\alpha}+l_r\cdot\ddot{\beta}\right)-l_l\cdot m_s\cdot\left(\ddot{y}_{srl}-\ddot{y}_b-l_b\cdot\ddot{\alpha}-l_l\cdot\ddot{\beta}\right)-l_l\cdot m_s\cdot\left(\ddot{y}_{sfl}-\ddot{y}_b+l_f\cdot\ddot{\alpha}-l_l\cdot\ddot{\beta}\right)+I_b\cdot\ddot{\beta}\\
+l_r\cdot c_{sfr}\cdot\left(\dot{y}_{sfr}-\dot{y}_b+l_f\cdot\dot{\alpha}+l_r\cdot\dot{\beta}\right)+l_r\cdot c_{srr}\cdot\left(\dot{y}_{srr}-\dot{y}_b-l_b\cdot\dot{\alpha}+l_r\cdot\dot{\beta}\right)-l_l\cdot c_{srl}\cdot\left(\dot{y}_{srl}-\dot{y}_b-l_b\cdot\dot{\alpha}-l_l\cdot\dot{\beta}\right)-l_l\cdot c_{sfl}\cdot\left(\dot{y}_{sfl}-\dot{y}_b+l_f\cdot\dot{\alpha}-l_l\cdot\dot{\beta}\right)\\
+l_r\cdot c_L\cdot\left(\dot{y}_{sfr}-\dot{y}_b+l_f\cdot\dot{\alpha}+l_r\cdot\dot{\beta}\right)+l_r\cdot c_L\cdot\left(\dot{y}_{srr}-\dot{y}_b-l_b\cdot\dot{\alpha}+l_r\cdot\dot{\beta}\right)-l_l\cdot c_L\cdot\left(\dot{y}_{srl}-\dot{y}_b-l_b\cdot\dot{\alpha}-l_l\cdot\dot{\beta}\right)-l_l\cdot c_L\cdot\left(\dot{y}_{sfl}-\dot{y}_b+l_f\cdot\dot{\alpha}-l_l\cdot\dot{\beta}\right)\\
+l_r\cdot k_{sfr}\cdot\left(y_{sfr}-y_b+l_f\cdot\alpha+l_r\cdot\beta\right)+l_r\cdot k_{srr}\cdot\left(y_{srr}-y_b-l_b\cdot\alpha+l_r\cdot\beta\right)-l_l\cdot k_{srl}\cdot\left(y_{srl}-y_b-l_b\cdot\alpha-l_l\cdot\beta\right)-l_l\cdot k_{sfl}\cdot\left(y_{sfl}-y_b+l_f\cdot\alpha-l_l\cdot\beta\right)\\
+l_l\cdot Bl\cdot\frac{U_{fl}}{R}\cdot\frac{i\cdot r_g}{r}+l_l\cdot Bl\cdot\frac{U_{rl}}{R}\cdot\frac{i\cdot r_g}{r}-l_r\cdot\frac{U_{fr}}{R}\cdot\frac{i\cdot r_g}{r}-l_r\cdot Bl\cdot\frac{U_{rr}}{R}\cdot\frac{i\cdot r_g}{r}=0\\
\\
L_e\cdot\frac{\dot{U}_{fr}}{R}+\frac{U_{fr}}{R}\cdot\left(R_e+R\right)=\frac{k_e\cdot i}{r}\cdot\left(\dot{y}_{sfr}-\dot{y}_b+l_f\cdot\dot{\alpha}+l_r\cdot\dot{\beta}\right)\\
\\
L_e\cdot\frac{\dot{U}_{fl}}{R}+\frac{U_{fl}}{R}\cdot\left(R_e+R\right)=\frac{k_e\cdot i}{r}\cdot\left(\dot{y}_{sfl}-\dot{y}_b+l_f\cdot\dot{\alpha}-l_l\cdot\dot{\beta}\right)\\
\\
L_e\cdot\frac{\dot{U}_{rr}}{R}+\frac{U_{rr}}{R}\cdot\left(R_e+R\right)=\frac{k_e\cdot i}{r}\cdot\left(\dot{y}_{srr}-\dot{y}_b-l_b\cdot\dot{\alpha}+l_r\cdot\dot{\beta}\right)\\
\\
L_e\cdot\frac{\dot{U}_{rl}}{R}+\frac{U_{rl}}{R}\cdot\left(R_e+R\right)=\frac{k_e\cdot i}{r}\cdot\left(\dot{y}_{srl}-\dot{y}_b-l_b\cdot\dot{\alpha}-l_l\cdot\dot{\beta}\right)
\end{array}
\right.
$$